

RESEARCH ARTICLE

10.1029/2017JB015366

Multiscale Insights Into Borehole Instabilities in High-Porosity Sandstones

Huanran Wu<sup>1</sup>, Jidong Zhao<sup>1</sup>, and Ning Guo<sup>2</sup>

Special Section:

Rock Physics of the Upper Crust

<sup>1</sup>Department of Civil and Environmental Engineering, Hong Kong University of Science and Technology, Clearwater Bay, Kowloon, Hong Kong, <sup>2</sup>Department of Civil and Environmental Engineering, Carleton University, Ottawa, Ontario, Canada

Key Points:

- A fully coupled FEM/DEM multiscale modelling approach was developed to simulate borehole instabilities in high-porosity sandstones
- Slot-like breakouts and other failure patterns were well captured, and underlying microstructure were identified
- Key factors, triggering conditions and critical micro-mechanisms pertaining to borehole breakouts were analysed by the multiscale framework

Correspondence to:

J. Zhao, jzhao@ust.hk

Citation:

Wu, H., Zhao, J., & Guo, N. (2018). Multiscale insights into borehole instabilities in high-porosity sandstones. *Journal of Geophysical Research: Solid Earth*, 123, 3450–3473. <https://doi.org/10.1029/2017JB015366>

Received 20 DEC 2017

Accepted 4 APR 2018

Accepted article online 17 APR 2018

Published online 8 MAY 2018

**Abstract** This paper presents a multiscale analysis of the classical borehole instability problem in high-porosity sandstones using a hierarchical multiscale approach. A rigorous, two-way message-passing coupling of finite element method and discrete element method is employed, where the finite element method is employed to solve a boundary value problem and the constitutive material responses required at each of its integration points are derived by the discrete element method solution to an embedded representative volume element instead of by using an assumed phenomenological model. We employ this multiscale approach to examine the successive failure of a borehole subjected to gradually decreased support stresses at the inner borehole wall or increased far-field stresses. To reproduce the material behavior of high-porosity sandstone, representative volume elements with a high-porosity structure and interparticle bonds are generated. It is found that stress concentration triggers the initial failure at the borehole wall, and the subsequent failure in form of deformation bands is driven by further stress concentration ahead of the band tips. The failure pattern around the borehole varies with initial stress state and global loading path. The comparison of the local stress paths of the initial failure points in various cases reveals that the change of failure pattern from shear failure to mixed-mode failure and to compaction failure is dominated by the increased mean stress. Cross-scale parametric studies show that the failure mode changes from clear compaction bands to multiple arrays of shear bands by changing the high-porosity specimen to a low-porosity one. The increase in cohesion strength expands the yield locus and enlarges the critical mean stress between different failure patterns. Hence, the failure mode may change from compaction failure to mixed-mode failure or from mixed-mode failure to shear failure due purely to the increased cohesion strength. The qualitative comparisons indicate greater length, larger area, and more severe damage of the diametrically opposite failure with the increase in minor principal stress  $\sigma_0$  and principal stress ratio. The diametrically opposite failure mode is found a good indicator for  $\sigma_0$  direction, but it may also occur under hydrostatic far-field stress due to material anisotropy.

1. Introduction

Borehole instabilities may cause adverse consequences for applications and operations in geotechnical investigation, mining, and hydrocarbon production, ranging from increased drilling time and cost, lost circulation, solid production, and even borehole collapse (Fjær et al., 2008). There have been extensive studies on borehole instability within an engineering context, focusing primarily on the determination of the optimum mud pressure to maintain the stability. Relevant theoretical and experimental investigations include the estimation of the stresses around a borehole and the evaluation of the critical conditions on borehole failures. The theories involved in relevant studies range from linear to nonlinear elasticity, isotropy to anisotropy, and various failure criteria on rocks. For example, isotropic elasticity and the well-known Kirsch equations have been combined in deriving the stresses around a borehole (Schmitt et al., 2012; Zoback et al., 1985). The solution has been generalized by introducing nonlinear elasticity (Ewy & Cook, 1990a; Santarelli, Brown, & Maury, 1986) and anisotropy of the material (Ong & Roegiers, 1993). The Biot theory has further been employed to consider the coupled poroelastic effects on the related solutions to the stresses (Detournay & Cheng, 1988; Haimson & Fairhurst, 1967). Within the same poromechanics framework, other influencing factors, such as the material anisotropy (Cui et al., 1996), the dual-porosity nature of fractured rocks (Zhang et al., 2003), and the thermal effects (Gelet et al., 2012), have also been examined on borehole stress fields.

Meanwhile, substantial efforts have been made to develop failure criteria for improved predictions of borehole failure over the frequently used Mohr-Coulomb criterion (Zervos et al., 2001; Zhang et al., 2003;

Zoback et al., 1985) and Drucker-Prager criterion (Bradley, 1979; Zhang et al., 2003). Particular emphases have been placed upon proper account of the material anisotropy (Ong & Roegiers, 1993; Zhang, 2013) and the strengthening effect of the intermediate principal stress (Al-Ajmi & Zimmerman, 2006; Haimson, 2002). Robust predictive constitutive models that provide all ranges of coverage, including the pure elastic deformation, plastic hardening, and failure and softening of a borehole instability problem, prove to be more desirable and effective and have been developed for borehole analysis (Ewy, 1993; Francois et al., 2014). The scale effect of localized failure of boreholes has also been investigated by nonconventional gradient elasto-plasticity (Zervos et al., 2001) and regularization based on fracture energy (Crook et al., 2003). The well-established bifurcation theory widely applied for material instability analysis (Papanastasiou & Vardoulakis, 1992) and the extension of preexisting fractures based on fracture mechanics (Germanovich & Dyskin, 2000; Shen et al., 2002) have also been employed to study the breakout of boreholes. More recent studies based on the discrete element method (DEM) focus particularly on revealing the micromechanisms of borehole failures in granular rocks (Al-Busaidi et al., 2005; Duan & Kwok, 2016; Fakhimi et al., 2002; H. Lee et al., 2016; Rahmati et al., 2014).

The borehole instability problem is commonly treated as an instantly created hole subjected to increasing far-field stresses (Crook et al., 2003; Cui et al., 1997; Zervos et al., 2001). Yet the failure of borehole may be induced by various factors and the failure patterns may depend crucially on the specific loading/stress path. For example, realistically replicating the drilling process of a borehole in a rock formation subjected to preexisting tectonic stresses can be critical to its potential failure analysis. Zheng et al. (1989) conducted boundary element analyses on the progressive failure around a borehole and discovered that the stable breakouts created in rock subjected to preexisting stresses are much larger than those created by increasing the far-field stresses to the same values. Hollow cylinder tests on Berea sandstones following different stress paths also verified the effects of stress path and the stress state (Ewy & Cook, 1990b). Laboratory drilling tests on Berea sandstones further indicated the possibility of different failure patterns corresponding to different sequences of hole creation and the application of far-field stresses (Haimson, 2003).

Borehole breakouts and the associated micromechanisms have been a focal topic of great interest. Thick-walled hollow cylinder tests and laboratory drilling experiments on rock have been conducted to examine the failure mechanisms of boreholes and to investigate the initiation and development of breakouts. According to these studies, V-shaped (dog-eared) breakouts are the most commonly observed patterns due to progressive extensile or shear failure of the borehole (Ewy & Cook, 1990b; M. Lee & Haimson, 1993; Santarelli & Brown, 1989). Interestingly, a distinct type of breakout, named as "fracture-like" breakouts by Haimson and Song (1998) or "slot-like" breakouts by others, has more recently been found extending from the borehole wall along the minor principal stress direction in the drilling experiments of high-porosity quartz-rich sandstones, such as high-porosity Berea sandstones (BSs22, porosity: 22% and BSs25, porosity: 25%; Haimson, 2001; Haimson & Kovacich, 2003; Haimson & Song, 1998), Mansfield sandstone (porosity: 26%; Haimson & Lee, 2004), and high-porosity St. Peter sandstone (porosity: 16–22%; Haimson & Klaetsch, 2007). Figure 1 illustrates both V-shaped and "fracture-like" breakouts observed in laboratory experiments on sandstones. The "fracture-like" pattern bears similarities to the "compaction band" observed in high-porosity sandstones, including their developing orientations (perpendicular to the maximum compressive stress), their contractive failure mechanisms, their host rock properties (high-porosity quartz-rich sandstone), and their almost constant bandwidth (5–10 grain diameters). Notably, however, the V-shaped breakouts developed in Tablerock sandstone (porosity:  $28 \pm 3\%$ ) as observed by Haimson and Lee (2004) appear to show that the degree of cementation may play a dominant role over the porosity in their occurrence, which was further supported by tests on sintered glass bead bricks (Bessinger et al., 1997).

Despite the extensive studies, there are many related issues remaining to be thoroughly addressed pertaining to borehole instabilities in sandstone. For instance, the dependency of borehole failure on loading or stress paths has not been fully recognized and understood. The forming conditions and failure mechanisms of more recently reported compaction bands around a borehole have not been investigated thoroughly. The correlations of porosity and interparticle cementation with breakout patterns have not been systematically investigated. Although some attempts have been made to interpret the failure mechanisms based on micrographs of the final failure patterns (Haimson, 2007; Haimson & Lee, 2004), direct particle-scale observations during the failure process are desired to understand the underlying micromechanisms. In an attempt to partially address these unsolved problems, we employ a recently developed hierarchical multiscale modeling

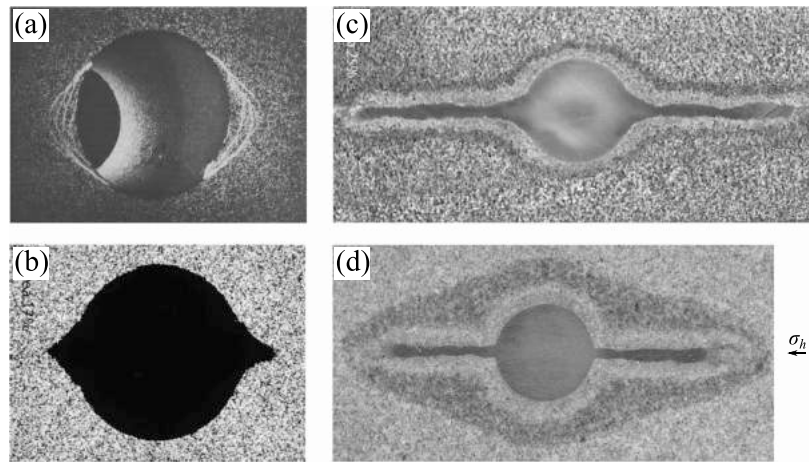


**Figure 1.** Examples of borehole breakouts observed in laboratory experiments on sandstones. (a) V-shaped breakouts in a Berea sandstone thick-walled hollow cylinder specimen (after Ewy & Cook, 1990a), (b) V-shaped breakouts in a Berea sandstone rectangular prismatic specimen (after Haimson, 2007), (c) “fracture-like” breakouts in Berea sandstone (after Haimson, 2007), and (d) “fracture-like” breakouts in Mansfield sandstone (see the developing orientation along the minor principal stress [ $\sigma_n$ ] direction, after Haimson & Lee, 2004).

approach based on rigorous finite element method (FEM) and DEM coupling (Guo & Zhao, 2014; Guo, Zhao, & Sun, 2016; see also Andrade et al., 2011; Desrues et al., 2015; Liu et al., 2016; Nitka et al., 2011) in this study to revisit the borehole instability problem in sandstone. In this multiscale scheme, FEM is used to solve the boundary value problem, whereby different loading/stress paths can be applied readily. A representative volume element (RVE) consisting of discrete element particles is embedded at each Gauss integration point of the FEM mesh. It receives the deformation gradient from the FEM solver as boundary conditions and derives the local material constitutive responses through direct DEM computations to feed the global FEM computations. The multiscale scheme offers great convenience in examining the effects of material properties from the microscale (grain scale), while avoiding unphysical, mostly complicated phenomenological constitutive assumptions in conventional continuum-based modeling approaches. Figure 2 presents a schematic illustration of the multiscale scheme in application to a borehole problem. A multiscale analysis of the borehole problem based on the fully coupled FEM/DEM approach may provide us with direct cross-scale information for macro-micro correlations for the entire borehole failure process and help fill the gap between the status quo continuum modeling of borehole breakouts and fundamental understanding in their underlying micromechanisms. In particular, special focuses of this study will be placed upon identifying the micromechanisms behind the compaction bands formed around a borehole, the discrepancy in failure mechanisms due to different loading paths, the clear influences of material properties including porosity and cohesion strength on the failure behaviors, and the correlation between the failure dimension and the far-field stresses.

## 2. Multiscale Analysis of Borehole Stability

In the hierarchical multiscale approach, the conventional constitutive relationship required for each Gauss integration point of the FE mesh is replaced by a two-way interactive RVE. The FEM passes the deformation information at each of its Gauss integration points to the corresponding RVE as boundary conditions, and then receives key material responses including tangent operator and stress from the DEM solution to the RVE as an embedded boundary value problem (see Figure 2). Since excessive repeat of the methodology itself may distract the focus of the study, the readers may refer to Guo and Zhao (2014) for detailed formulations and solution procedure of the approach. In what follows, we only present the ingredients relevant to multiscale modeling of a typical borehole problem.

### 2.1. Borehole Stability Analysis

A typical borehole problem is simplified as a ring with an inner borehole radius  $r_i = 15$  mm and an outer radius  $r_o = 150$  mm by assuming plane strain conditions (Figure 3a). Although a rectangular outer boundary is

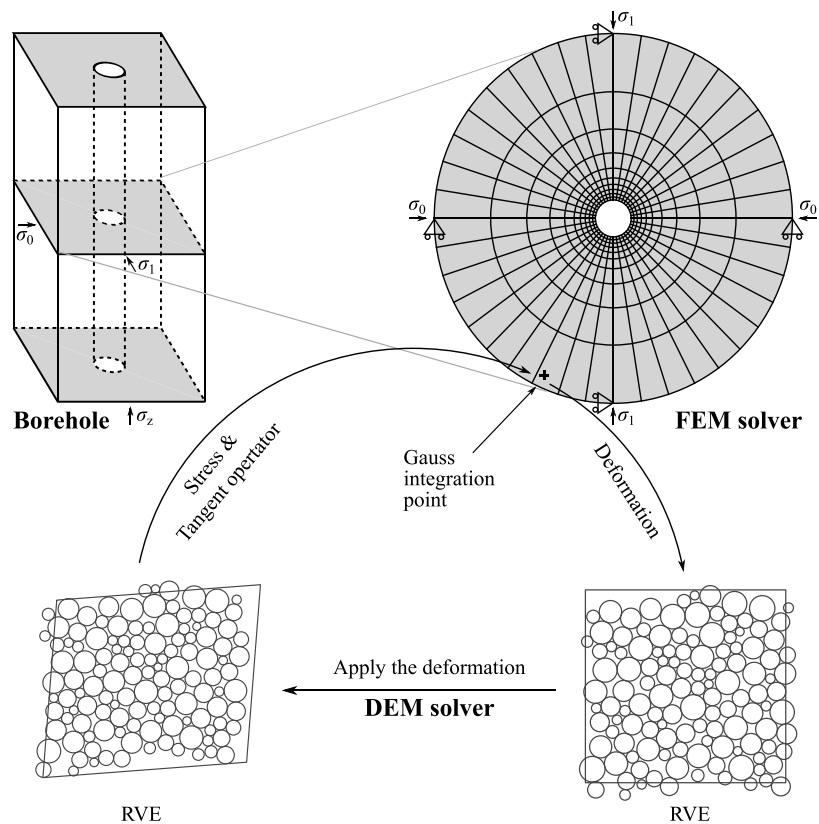


**Figure 2.** Illustration of the coupled finite element method/discrete element method hierarchical multiscale modeling approach for borehole stability analyses. The outer boundary of the domain is circular to achieve an idealized axisymmetric mesh. Detail on the boundary conditions is presented in Figure 3.

commonly adopted for unequal far-field stresses (e.g., the minor principal stress  $\sigma_0$  is smaller than the major principal stress  $\sigma_1$ ), a circular domain is adopted here to help regularize and simplify the mesh discretization. Indeed, Papanastasiou and Vardoulakis (1992) have used the ring domain to analyze the borehole failure under unequal far-field stresses. Nonhydrostatic stresses are applied on the circular inner boundary as well, which simulates the decreasing of the inner stresses from their in situ condition during the drilling process. By applying the same nonhydrostatic stresses on both the outer and inner boundaries, we are able to set the same initial stress state for all the RVEs in the domain, which satisfies the equilibrium condition and eases the preparation of the initial RVE packing. The domain is divided into  $80 \times 20$  (the hoop direction  $\times$  the radial direction) eight-node quadrilateral elements each with four Gauss integration points. A finer mesh is generated close to the borehole wall. The discretization and prescribed boundary conditions are presented in Figure 3a.

The borehole in this study is modeled by considering the far-field stresses ( $\sigma_0, \sigma_1$ ) and the inner stresses ( $\sigma_{i0}, \sigma_{i1}$ ). Given the dependency of failure patterns on loading/stress paths, three different loading paths are taken into consideration as shown in Figures 3b–3d, where stress quantities are normalized by final minor principal stress  $\sigma_{f0}$  and the pseudo time  $T$  (loading steps) is normalized by the total simulation steps  $T_T$ . Note that the final stress ratio ( $\sigma_1/\sigma_0 = 1.5$ ) in Figures 3b–3d is just for convenient illustration and may be different than 1.5 (for Cases V, VIII, and IX). Decreasing inner stresses is considered to be a good approximation of real drilling process, during which the rock mass in the borehole is removed and the inner boundary of the borehole becomes unsupported (Ewy, 1993). Paths i and ii are designed to induce borehole failure under unequal far-field stresses. Increasing far-field stresses to cause the borehole failure is the common stress path in thick-walled hollow cylinder tests (Cuss et al., 2003; Dresen et al., 2010). Path iii is designed to simulate these tests, and  $\sigma_1$  is further increased to reach the same final state as the previous two. Specifically, the three stress paths are designed as follows: (1) Path i:  $\sigma_{i1}$  is reduced at a constant rate, while  $\sigma_{i0}$  is kept unchanged, until  $\sigma_{i1}$

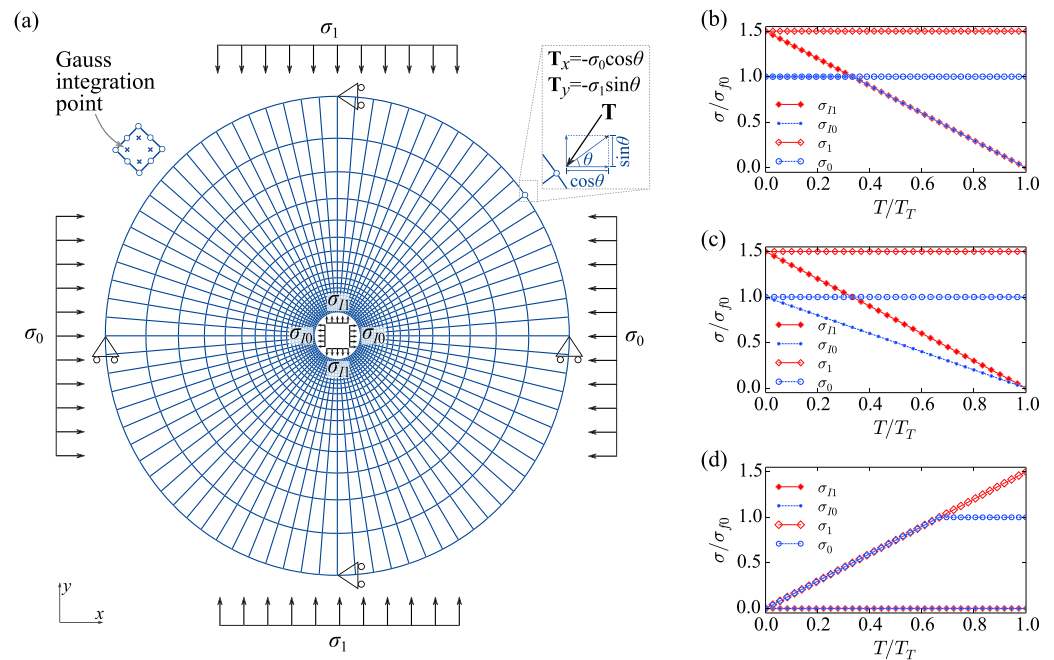


**Figure 3.** (a) Finite element discretization by eight-node quadratic quadrilateral elements with four integration points (reduced integration to reduce the computation time) and the prescribed boundary conditions for the borehole analyses. Three different global loading paths, (b) path i, (c) path ii, and (d) path iii, for failure pattern analyses. The nonhydrostatic stresses on the inner and outer circular boundaries are applied by traction forces on the boundary nodes, where the traction force vector  $\mathbf{T} = -\boldsymbol{\sigma} \cdot \mathbf{n}$ ,  $\boldsymbol{\sigma}$  being the stress tensor and  $\mathbf{n}$  being the outward normal of the boundary surface.

is reduced to be equal to  $\sigma_{10}$ . After that,  $\sigma_{10}$  and  $\sigma_{11}$  are further reduced to zero at the same rate. The far-field stresses  $\sigma_1$  and  $\sigma_0$  are kept constant. (2) Path ii: Both  $\sigma_{10}$  and  $\sigma_{11}$  are reduced proportionally to zero. The far-field stresses  $\sigma_1$  and  $\sigma_0$  are kept constant. (3) Path iii: The inner support stresses are set zero during the whole loading process, while the far-field stresses  $\sigma_0$  and  $\sigma_1$  are increased to induce the failure of the borehole. It is noteworthy to mention that all following simulations and analyses are based on continuum mechanics for the macrodomain. No attempt is made here to simulate discontinuous behavior such as fracturing or dislocation, though they may be discussed in relation with our results. The inner support stresses are related to the in situ support of the rocks in the hole, which will be removed during the drilling process (modeled by decreasing  $\sigma_{10}$  and  $\sigma_{11}$  in the study). Neither pore pressure nor fluid flow is involved in this study.

## 2.2. RVE With High-Porosity Structure

In laboratory drilling tests, intact grains repacking to a lower porosity with little intragranular fracturing have been observed in the narrow zone ahead of the “fracture-like” breakout in high-porosity Berea sandstone (BSs25; Haimson, 2003). Compared to the cases of compaction bands, although severe particle crushing has been observed in compaction bands reproduced in laboratory triaxial compression tests on sandstones (Baud, Klein, & Wong, 2004), field observations indicate much fewer and significantly less intense grain crushing (Aydin & Ahmadov, 2009). This arouses the question of whether or not compaction bands can be formed in the absence of grain crushing. A recent multiscale numerical study by the authors Wu, Guo, and Zhao (2017) has indeed reproduced compaction bands in biaxial compressions of high-porosity sandstones where no particle crushing mechanism is involved. The present study employs a similar high-porosity structure as used in this early study to examine the characteristic of compaction bands around a borehole in high-porosity quartz-rich sandstone without considering grain crushing. We note, however, that the high-porosity structure may be one of many possible microstructures in sandstone that trigger compaction bands.

The high-porosity structure is considered to simulate the microstructure in sandstones where some macropores present a shape and a size resembling that of grains. These grain-like macropores may have been

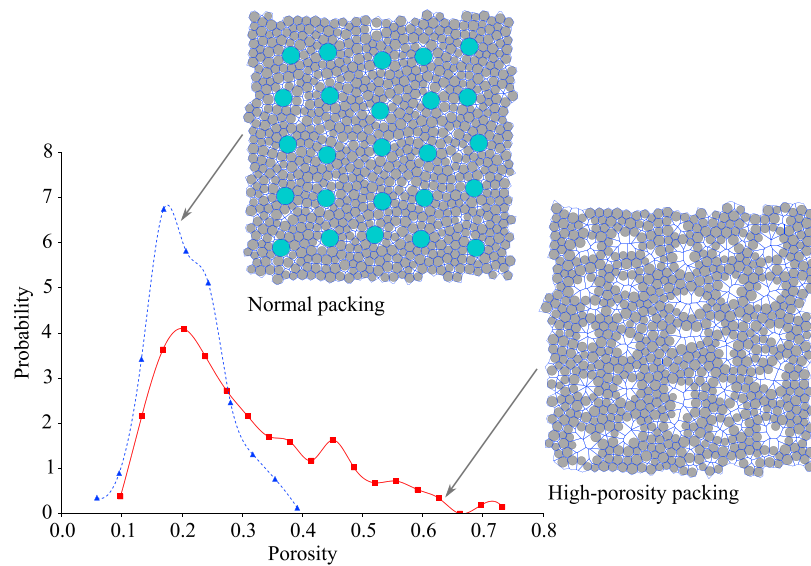


**Figure 4.** The local porosity distributions of the high-porosity packing and the normal packing. Voronoi tessellations of the corresponding packing are shown as insets. The blue particles are preinserted larger particles, and the gray ones are those of normal radii.

formed due to the weathering out of feldspar grains or other processes (Baud et al., 2015; Charalampidou et al., 2014). The RVE packing with high-porosity structure is prepared by removing some preinserted larger particles and rattlers (particles with less than one contact). Normal and tangential bonds are applied to interparticle contacts before the removal to maintain the stability of the structure.

The Voronoi cell is then employed to compute the local porosity of the RVE packing. Since each Voronoi cell contains exactly one particle, the porosity is easily obtained from the volume (area in 2-D) of the particle and the corresponding cell. Figure 4 demonstrates the comparison of the local porosity distribution between the high-porosity packing and the normal packing before the removal of any particles. It is easy to observe the notable decrease in the low-porosity portion and the increase in the high-porosity portion in the high-porosity packing. The high-porosity packing (2-D) demonstrated in Figure 4 has an overall porosity of 0.323.

For simplicity, a bonded contact model with linear force-displacement contact law and a Coulomb-type friction criterion is employed here. The typical microparameters adopted are summarized in Table 1. The radii of the particles are linearly distributed from 0.2 to 0.3 mm. A particle density of 2,650 kg/m<sup>3</sup> and an interparticle friction angle of 35° are common in DEM modeling of sands and sandstones and are adopted here. Two user-defined parameters  $E_c$  and  $\nu_c$  are involved to derive the normal ( $k_n$ ) and the tangential ( $k_t$ ) contact stiffnesses as  $k_n = E_c r^*$  and  $k_t = \nu_c k_n$ , where  $r^* = 2r_1 r_2 / (r_1 + r_2)$ , and  $r_1$  and  $r_2$  are the radii of the two contacted particles. Another parameter  $c$  (denoted as cohesion strength in the study) is adopted to define the maximum tensile force as  $F_n^{\max} = c \min(r_1, r_2)^2$  and the maximum tangential force as  $F_t^{\max} = c \min(r_1, r_2)^2 + F_n \tan \phi$ .  $E_c$ ,  $\nu_c$ , and  $c$  are calibrated based on a uniaxial compressive strength (UCS) of 24.9 MPa and Young's modulus of 11.0 GPa for sandstone. For comparison, the BSs25 sandstone has a UCS of  $24 \pm 2$  MPa (Haimson & Kovacich, 2003). The Mansfield sandstone (porosity:  $26 \pm 1\%$ ), wherein "fracture-like" breakouts were also observed, has a UCS of  $22.4 \pm 0.5$  MPa and Young's modulus of  $9.6 \pm 0.1$  GPa (Haimson & Lee, 2004).

**Table 1**  
Typical Microparameters for the Representative Volume Element

Radii (mm)	Particle density (kg/m <sup>3</sup> )	$E_c$ (GPa)	$\nu_c$	Friction angle $\phi$ (°)	$c$ (GPa)
0.2–0.3	2,650	950	1.0	35	6.8

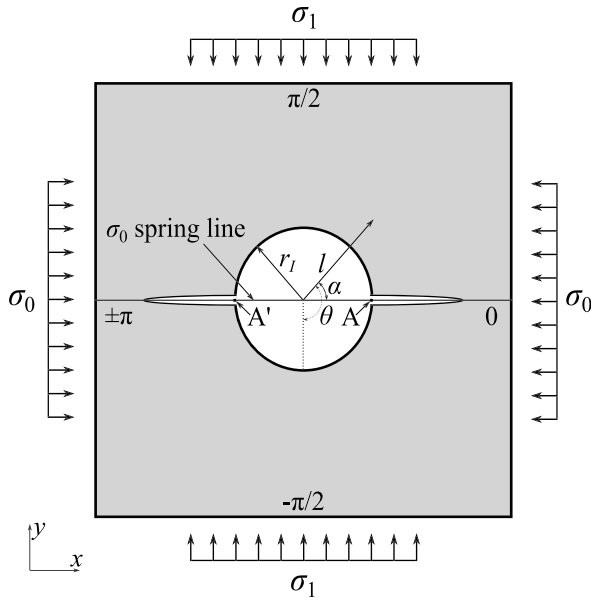


**Figure 5.** Schematic diagram for compaction bands around a borehole.  $\sigma_0$  spring line aligns along the diameter parallel to  $\sigma_0$ . Counterclockwise is taken as positive for the polar coordinate  $\alpha$ .

### 2.3. Validation of the Numerical Model

Conventionally, the stress distribution around a borehole subjected to major and minor far-field principal stresses ( $\sigma_H$  and  $\sigma_h$ ) can be derived by the Kirsch equations assuming isotropic elasticity as follows (Fjær et al., 2008; Haimson, 2007; Zoback et al., 1985):

$$\begin{aligned}\sigma_{rr} &= \frac{\sigma_H + \sigma_h}{2} \left(1 - \frac{r_l^2}{r^2}\right) + \frac{\sigma_H - \sigma_h}{2} \left(1 - 4\frac{r_l^2}{r^2} + 3\frac{r_l^4}{r^4}\right) \cos 2\theta + \Delta P \frac{r_l^2}{r^2} \\ \sigma_{\theta\theta} &= \frac{\sigma_H + \sigma_h}{2} \left(1 + \frac{r_l^2}{r^2}\right) - \frac{\sigma_H - \sigma_h}{2} \left(1 + 3\frac{r_l^4}{r^4}\right) \cos 2\theta - \Delta P \frac{r_l^2}{r^2} \\ \tau_{r\theta} &= -\frac{\sigma_H - \sigma_h}{2} \left(1 + 2\frac{r_l^2}{r^2} - 3\frac{r_l^4}{r^4}\right) \sin 2\theta\end{aligned}\quad (1)$$

where  $\sigma_{rr}$ ,  $\sigma_{\theta\theta}$ , and  $\tau_{r\theta}$  are the radial, tangential, and shear stresses, respectively;  $r_l$  is the radius of the borehole;  $l$  is the distance from the center of the borehole;  $\theta$  is the angular direction measured counter clockwise from the  $\sigma_H$  direction (i.e.,  $\theta = \alpha + \pi/2$ , see Figure 5 for illustration); and  $\Delta P$  is the difference between the fluid pressure in the borehole and the pore pressure in the rock (ignored in this study).

Stress distribution around the borehole at the prefailure stage of Case I (see the detailed setup in Table 2) is employed as a validation of the numerical model. In this case, compaction bands developed along the  $\sigma_0$  spring line (see Figure 7) when decreasing the inner support stresses gradually follow-

ing Path i. A sketch of compaction bands around a borehole is illustrated in Figure 5 showing the far-field stresses, the  $\sigma_0$  spring line, and its intersection points A and A' with the borehole wall. The prefailure stresses could be obtained by superposing the Kirsch solution for an unsupported borehole subjected to far-field stresses of  $\sigma_H = \Delta\sigma_1 = \sigma_1 - \sigma_{I1}$  and  $\sigma_h = \Delta\sigma_0 = \sigma_0 - \sigma_{I0}$  and the in situ stresses of a fully supported borehole (the support stresses are in balance with the far-field stresses) subjected to far-field stresses of  $\sigma_{yy} = \sigma_{I1}$  and  $\sigma_{xx} = \sigma_{I0}$ . The stress components in the Cartesian coordinate system could be transformed into the polar coordinate system with the following equations (Duan & Kwok, 2016):

$$\begin{aligned}\sigma_{rr} &= \sigma_{xx} \cos^2 \alpha + \sigma_{yy} \sin^2 \alpha + 2\tau_{xy} \sin \alpha \cos \alpha \\ \sigma_{\theta\theta} &= \sigma_{xx} \sin^2 \alpha + \sigma_{yy} \cos^2 \alpha - 2\tau_{xy} \sin \alpha \cos \alpha \\ \tau_{r\theta} &= (\sigma_{yy} - \sigma_{xx}) \sin \alpha \cos \alpha + \tau_{xy} (\cos^2 \alpha - \sin^2 \alpha)\end{aligned}\quad (2)$$

where  $\sigma_{xx}$ ,  $\sigma_{yy}$ , and  $\tau_{xy}$  are the stress components in the Cartesian coordinate system and  $\alpha$  is the angular direction from  $x$  axis ranging from  $-\pi$  to  $\pi$  (see Figure 5 for illustration).

**Table 2**  
Summary of Cases for the Borehole Stability Analyses

Case no.	Particle number	Initial porosity	$c$ (GPa)	$\sigma_0$ (MPa)	$\sigma_1$ (MPa)	Loading path <sup>a</sup>	Description
I	749	0.325	6.8	40	60	i	CB, thickened in width
II	749	0.326	6.8	40	60	ii	CB, thickened in width
III	749	0.326	6.8	30	45	i	CB and SB (appear after CB)
IV	749	0.326	6.8	30	45	ii	MM and SB
V	749	0.327	6.8	20	35	i	MM and SB
VI	749	0.329	6.8	30	45	iii	Diffuse shear failure
VII	749	0.327	6.8	20	30	i	SB
VIII	749	0.327	6.8	20	40	i	MM and SB
IX	749	0.326	6.8	40	40	i	SB
X	749	0.326	9.0	30	45	i	MM and SB
XI	749	0.327	4.5	20	30	i	MM and SB
XII	736	0.279	6.8	40	60	i	SB

Note. CB: compaction band; SB: shear band; MM: mixed-mode failure.

<sup>a</sup>Refer to Figure 3 for the specified loading paths.

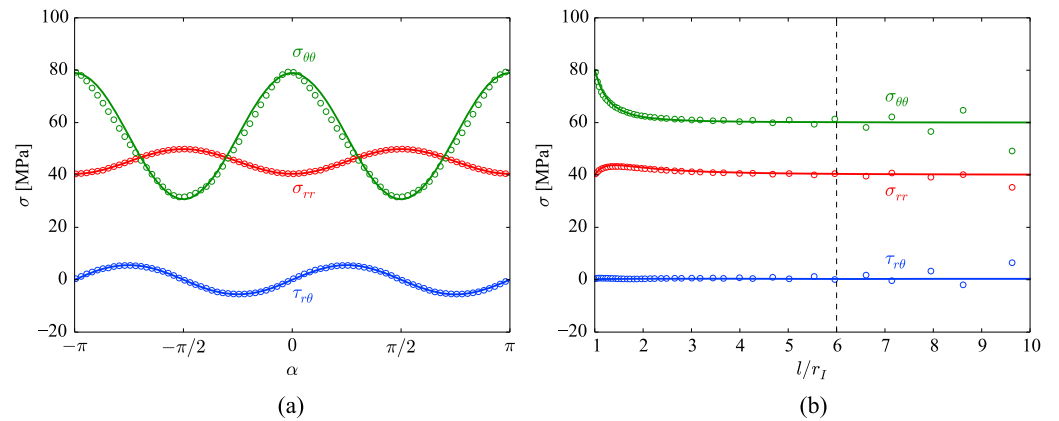


**Figure 6.** Comparison between the stresses obtained from the multiscale simulations (open circles) and the analytical solutions (solid lines) (a) around the borehole wall and (b) along the  $\sigma_0$  spring line.

Comparison between the analytical solutions and the stresses obtained from the multiscale simulations when  $T = 8$  (i.e.,  $\sigma_1 = 60$  MPa,  $\sigma_0 = 40$  MPa,  $\sigma_{11} = 50$  MPa, and  $\sigma_{10} = 40$  MPa) has been displayed as Figure 6. Figure 6a shows the stress distributions around the borehole wall. The measured stresses in the simulation agree well with the analytical solutions. Figure 6b shows the stresses along the  $\sigma_0$  spring line. The measured stresses from the multiscale model agree very well with the analytical solutions within  $6r_l$ . The deviation is due to the discretization error and the boundary constrain at  $l = 10r_l$ .

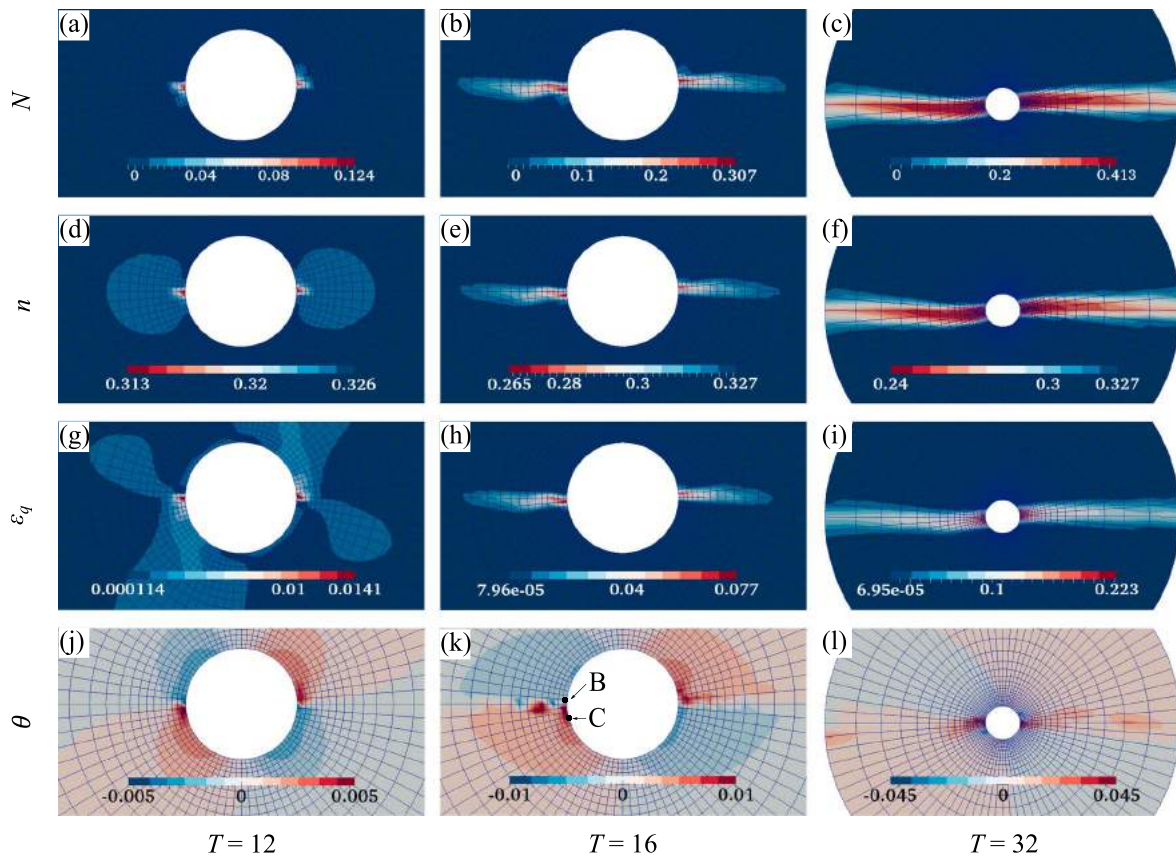


**Figure 7.** Zoomed views of the initiation and propagation of compaction bands around a borehole in high-porosity specimen (case I,  $\sigma_0 = 40$  MPa and  $\sigma_1 = 60$  MPa) in terms of the normalized debonding number ( $N$ ), the porosity ( $n$ ), the deviatoric strain ( $\epsilon_q$ ), and the average particle rotation ( $\theta$ ). The support stresses  $\sigma_{10}$  and  $\sigma_{11}$  are reduced following loading path i.

### 3. Initiation and Propagation of Borehole Failure

To investigate the initiation and the development of compaction bands around a borehole in high-porosity sandstones and the impact factors that control the failure patterns, we choose a set of 12 cases for the borehole stability analyses. Detailed setup of each test and a brief description of the observed failure patterns are summarized in Table 2. Among the 12 cases, Case I will be considered as a primary case for multiscale analysis, while the remaining cases will be employed as parametric studies on the controlling factors for borehole failure.

#### 3.1. Initiation and Propagation of Compaction Bands Around a Borehole

To demonstrate the initiation and subsequent propagation of compaction bands around a borehole, the multiscale predictions for case I with far-field stresses  $\sigma_0 = 40$  MPa,  $\sigma_1 = 60$  MPa are presented in Figure 7. The progressive failure of the borehole is caused by gradually reducing the support stresses  $\sigma_{11}$  and  $\sigma_{10}$ , following Loading Path i as illustrated in Figure 3b at a rate of 1.25 MPa per quasi-static loading step. The “fracture-like” breakout was reported in laboratory drilling experiments on Mansfield sandstone under the same far-field stress state (Haimson & Lee, 2004). In the drilling experiments, only the final pattern of the breakout was recorded. The failure mechanism has further been suggested from the microscale observations of thin sections of the breakouts with scanning electron microscope. One major focus of the present multiscale study is attempting to fill the gap of understanding from the initiation to the final pattern of the breakout based on direct cross-scale analyses.

We employ a combination of four variables to characterize the failure patterns of borehole: (1) the normalized debonding number ( $N$ ), that is, the debonding number normalized by the initial contact number in an RVE packing. It is comparable to the acoustic emission events commonly recorded in experiments and is employed here as an indicator of the damaging process; (2) the porosity ( $n$ ); (3) the deviatoric strain:

$\epsilon_q = \sqrt{(\epsilon_{xx} - \epsilon_{yy})^2 + 4\epsilon_{xy}^2}$ ; and (4) the average particle rotation:  $\theta = \sum_{N_p} \theta_p / N_p$ , where  $N_p$  is the number of particles within the packing and  $\theta_p$  is the accumulated rotation of individual particle. Counterclockwise rotation is taken as positive.

1. Initiation: The inception of localized failure of the borehole begins at a pseudo time (loading step)  $T = 12$  when  $\sigma_{10} = 40$  MPa and  $\sigma_{11} = 45$  MPa. The corresponding failure patterns in terms of  $N$ ,  $n$ ,  $\epsilon_q$ , and  $\theta$  are shown as the first column in Figure 7. Note that no progressive removal of grains is involved in this study. There are apparent debonding events occurring first at the intersection points (Points A and A') of the borehole wall with the  $\sigma_0$  spring line, and their porosity is reduced to a minimum of 0.313, while the porosity of elsewhere in the host rock slightly increases from the initial value of 0.325 to 0.326. The initiation of the compaction bands diametrically opposite from the borehole wall agrees with the prediction based on continuum model (Muller et al., 2011). The compaction at the two points causes stress relaxation there and the propagation of stress concentration. The associated stress paths will be analyzed later. While the deviatoric strain contour shows a consistent pattern with debonding and porosity, the contour of  $\theta$  displays an apparent characteristic of compaction band that the rock mass outside starts to rotate toward in the band (notice the sign of the rotation and the intensification near Points A and A'). The noticeable deviatoric strain and particle rotation within the compaction bands have been confirmed in our early multiscale biaxial compression simulations which rectified a common misleading impression that a compaction band contains only volumetric contraction (Wu et al., 2017).
2. Propagation and maturation: The mature pattern of compaction band at  $T = 16$  is presented as the second column in Figure 7 when  $\sigma_{10} = \sigma_{11} = 40$  MPa. With further reduction in  $\sigma_{11}$ , the bands propagate and penetrate farther into the host rock from Points A and A' along the  $\sigma_0$  spring line. The lengths of the bands become longer, while their widths keep almost unchanged. A mild curvature of the compaction bands is noticeable in Figures 7b, 7e, and 7h, which persists to the postmature stage (see Figures 7c, 7f, and 7i). This is possibly caused by a competition between the material anisotropy and the stress concentration. The degree of damage (in terms of  $N$ ) and the reduction of porosity near the borehole wall are both significantly more intense than that in the first column. Up to 30% of the contact bonds in the RVEs near Points A and A' are broken. The minimum porosity in the compaction band reaches 0.265, while the porosity in the host rock slightly increases to 0.327. “Fracture-like” breakouts have been observed in laboratory drilling experiments on BSs25 and Mansfield sandstones which consist of more than 85% quartz and

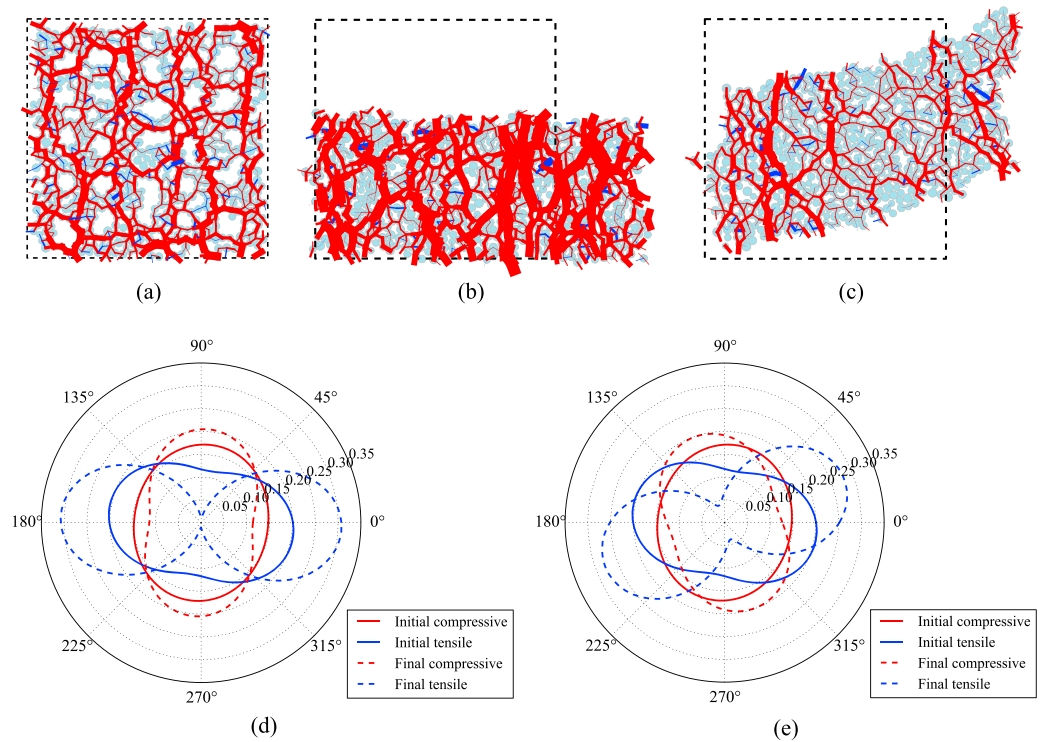


**Figure 8.** Force chain networks of the representative volume elements at (a) the initial state and the final stage of (b) point B and (c) point C (see Figure 7k for the positions of points B and C). The rose diagrams show the evolution of fabric anisotropy for (d) point B and (e) point C. In (a)–(c), the dotted squares indicate the initial position of the corresponding packing. The short lines indicate the interparticle normal contact forces. The thickness of the line is proportional to the magnitude of the normal contact force. The red lines stand for compressive contacts, and the blue ones represent tensile contacts.

are poorly cemented primarily by sutured grain contacts (Haimson & Kovacich, 2003; Haimson & Lee, 2004). In these experiments, a central vertical hole was drilled in a rectangular prismatic specimen subjected to true triaxial stress state and unpressurized drilling fluid was used to cool the bit and remove debris. The breakout width was found to be 5–10 average grain diameters, regardless of the test variables (Haimson & Kovacich, 2003; Haimson & Lee, 2004). Moreover, the 2-D porosity measured ahead of the breakout tip was smaller than that of the host rock, revealing a contractive failure mechanism (Haimson & Lee, 2004). In view of the great similarities, the “fracture-like” breakouts have therefore been regarded as emptied compaction bands (Haimson & Kovacich, 2003); that is, part of the compacted band was removed by the drilling fluid for the breakout with only a compacted zone ahead of the breakout tip left. The observed breakout length can be affected by the flow rate and the property of the drilling fluid such as unit weight (Sheets & Haimson, 2004). It is likely that the property of the drilling fluid controls the minimum degree of damage above which the rock mass is removable.

3. Postmature failure: The failure pattern at  $T = 32$  when  $\sigma_{10} = \sigma_{11} = 20$  MPa is shown as the third column in Figure 7. Further decrease in the support stresses leads to a continuous penetration of the compaction band into the host rock before reaching the outer boundary. The postmature propagation of bands accompanies with thickening bandwidth. Consistently, the contours of  $N$ ,  $n$ , and  $\epsilon_q$  help to identify a thicker band along the  $\sigma_0$  direction. In particular, the change of rotation patterns near the borehole wall is interesting to discuss. As mentioned before, during the compaction banding stage, the bandwidth is narrow compared to the borehole size, and a rotating-into-band pattern from outside the band is observed. The absolute boundary between clockwise and counterclockwise rotations twists along the band. However, as the band grows thicker entering postmature stage, the in-band rotations become dominant. Although a clear shear band is not observed, the  $\epsilon_q$  reaches a maximum of 0.223 near the borehole wall, about 3 times of that of the mature compaction band discussed above. Meanwhile, the minimum

- porosity is 0.240 as compared to a minimum of 0.264 in the mature compaction band stage. Evidently, entering the postmature deformation stage, the failure pattern has changed from a compaction dominated to a shear dominated one near the borehole wall. The deviatoric strain  $\epsilon_q$  is almost tripled, while the volumetric strain only marginally increases. Similar phenomena have also been observed in our early multiscale biaxial compression simulation of compaction bands (Wu et al., 2017). They are also consistent with the predictions based on continuum elastoplasticity models (Issen & Rudnicki, 2000; Olsson, 1999).
4. Evolution of microstructure: The multiscale approach facilitates direct connections of the macroscopically observed failure patterns with their microstructural origins. To demonstrate the associated microstructural changes during the formation of compaction bands, we compare the force chain networks of selected RVEs at the initial and the final stages in Figure 8. The force chain network of RVE packing at the initial state, shown in Figure 8a, is rather homogeneous with clear embedded macropores. Toward the final stage, as shown in Figures 8b and 8c, almost all macropores disappear due to pore collapse. In particular, the contact force network at Gauss Point B (close to Point A' as marked in Figure 5) indicates a nearly 50% compression along the vertical direction while being elongated around 30% horizontally, turning an initially square-shaped RVE into a rectangular one. The dominant strong force chains align in the vertical direction. Further corroborations can be provided by the rose diagram of anisotropy (defined by contact normal, see Guo & Zhao, 2013) for both tensile and compressive contacts, as shown in Figure 8d for the RVE at Gauss Point B. Evidently, the anisotropy of tensile contacts is intensified along the horizontal direction during the failure, while its increase in the compressive contacts is relatively mild. Since the vertical deformation is mainly caused by pore collapse rather than by the establishment of a considerable number of new compressive contacts, the mild increase in compressive contact anisotropy is reasonable. Meanwhile, since Point B is at the edge of borehole surface along the  $\sigma_0$  spring line, the relaxation of inner stresses results in inward movement and thus horizontal tensile deformation for Point B, which mobilizes substantially more tensile contacts to join to balance. In contrast, Figure 8c shows the final contact force network of the Gauss point C (Marked in Figure 7k) below Point A with  $\alpha \approx -166^\circ$ . The final geometry of a rough parallelogram and the overall counterclockwise rotation strongly indicate a shearing response. Most strong force chains in the network align perpendicular to the long edge of the parallelogram. Both anisotropy quantities rotate from its original orientation counterclockwise due to shear, where the rotation of tensile-contact anisotropy causes it to align along the long edge of the parallelogram and the anisotropy of compressive contact rotates to the perpendicular direction, as shown in Figure 8e. The increase in both anisotropies is not as intense as Point B.

### 3.2. The Role of Stress Concentration

It is interesting to examine the correlations between stress concentration around the borehole with the initiation and propagation of compaction bands. The computed stress distribution before localization (at  $T = 8$ ) in terms of  $p$  and  $q$  is shown in Figures 9c and 9e, where  $p = \frac{\sigma_{xx} + \sigma_{yy}}{2}$  is the mean stress (normalized by the far-field mean stress  $p_0 = 50$  MPa in Case I) and  $q = \sqrt{(\sigma_{xx} - \sigma_{yy})^2 + 4\sigma_{xy}^2}$  is the deviatoric stress (normalized by the far-field deviatoric stress  $q_0 = 20$  MPa in Case I). Figure 9a indicates that there is almost no damage occurring in the sandstone, while the reduction in support stresses causes apparent stress concentrations around the borehole wall. The concentration of mean stress  $p$  is mild, forming a shape of "∞" (Figure 9c), whereas the concentration of deviatoric stress  $q$  is rather intense in the vicinity of the borehole wall, presenting a butterfly shape (Figure 9e). Indeed, along  $\sigma_0$  spring line, the concentration of  $q$  decays quite fast, while the concentration effect of  $p$  is more far-reaching (see detailed stress paths in Figure 10). The most intense stress concentration near Points A and A' (see Figure 5) leads to the initiation of compaction bands, and the concentration continues to play a controlling role in their further propagation. The stress concentration after the propagation of the compaction bands is illustrated in the second column of Figure 9 (at  $T = 16$ , cf. the second column of Figure 7). High compressive stress concentrations cause interparticle debonding and pore collapse in relevant RVEs, which leads to stress relaxation in the compaction bands and, meanwhile, the propagation of the concentration to the tips of the bands. The stress release of  $p$  is localized in the band region (Figure 9d), while the stress release of  $q$  forms a wider weaving-shuttle-like shape along the  $\sigma_0$  spring line (Figure 9f). The new concentration of  $p$  in front of the band tip is limited in a small dumbbell shape region, while the new concentration of  $q$  forms a clear butterfly shape.

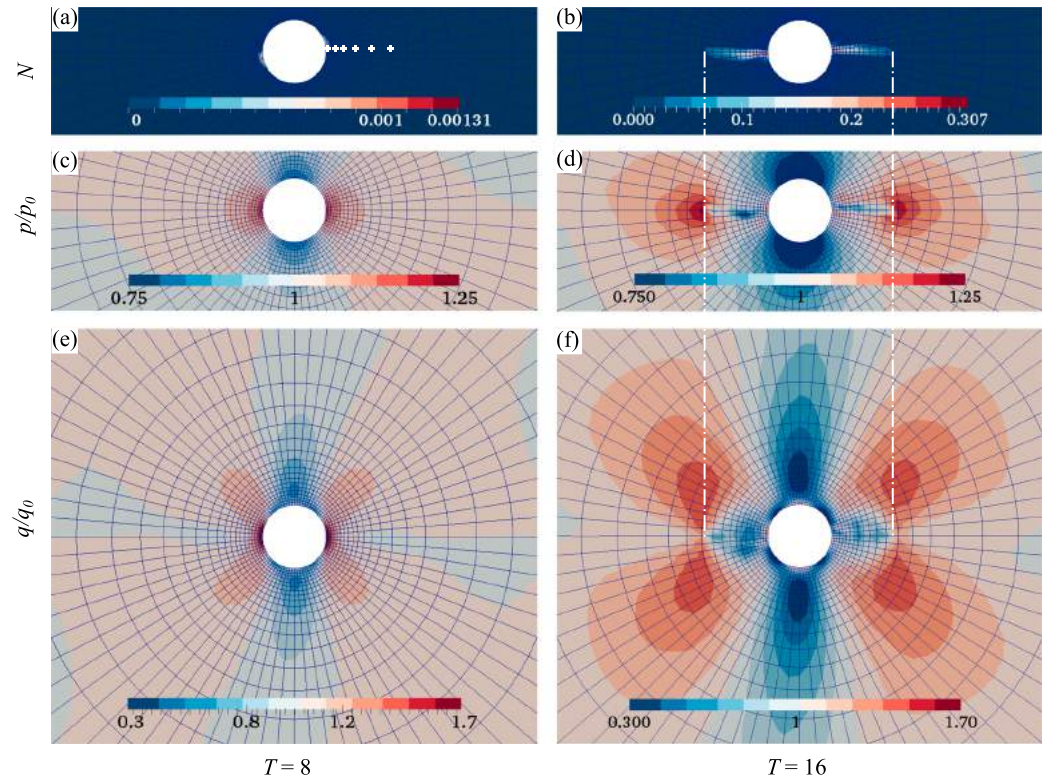


**Figure 9.** Zoomed views of the stress concentration around the borehole at different stages of compaction bands (different failure degrees in terms of normalized debonding number  $N$ ) in terms of mean stress  $p$  normalized by the far-field mean stress  $p_0$  and deviatoric stress  $q$  normalized by the far-field deviatoric stress  $q_0$  (case I, see the initiation and propagation of the failure in Figure 7). The first column is for prefailure stage at  $T = 8$  when  $\sigma_{11} = 50$  MPa and  $\sigma_{10} = 40$  MPa due to the reduction of support stresses. The second column is for mature stage at  $T = 16$  when  $\sigma_{11} = \sigma_{10} = 40$  MPa after the propagation of compaction bands.

Figure 10 further shows the evolution of volumetric strain  $\epsilon_v = \epsilon_{xx} + \epsilon_{yy}$  and stress concentrations over pseudo time for selected Gauss points along the  $\sigma_0$  spring line (marked as white points in Figure 9a). Evidently, prior to the initiation of compaction bands, the elastic  $\epsilon_v$  is negligibly small as compared to its postfailure magnitudes. As the support stresses are reduced,  $p$  and  $q$  around the borehole wall gradually increase. The dashed vertical line marks the initiation of the compaction bands at  $T = 12$ . The four dotted vertical lines mark the time sequence of the development of the band. It is interesting to note that the initiation of the pore collapse (surge of  $\epsilon_v$ ) and the stress drop ( $p$  and  $q$ ) of the same Gauss point occur at the same time, while  $p$  and  $q$  of the Gauss point ahead of the band tip undergo a sudden increase, which is corresponding to the stress concentration shown in Figures 9d and 9f. The stress relaxation in the band and the stress concentration ahead of the band tip develop successively along the  $\sigma_0$  spring line in sync with the propagation of the band.

The stresses at the prefailure stage along the  $\sigma_0$  spring line where  $\alpha = 0$  (i.e.,  $\theta = \pi/2$  in equation (1)) can be obtained by superposing the Kirsch solution (equation (1)) for an unsupported borehole subjected to far-field stresses of  $\sigma_H = \Delta\sigma_1 = \sigma_1 - \sigma_{11}$  and  $\sigma_h = \Delta\sigma_0 = \sigma_0 - \sigma_{10}$  and the in situ stresses of a fully supported borehole (the support stresses are in balance with the far-field stresses) subjected to far-field stresses of  $\sigma_{yy} = \sigma_{11}$  and  $\sigma_{xx} = \sigma_{10}$  as follows:

$$\begin{aligned} \sigma_{xx} &= \frac{\Delta\sigma_1 + \Delta\sigma_0}{2} \left( 1 - \frac{r_I^2}{r^2} \right) - \frac{\Delta\sigma_1 - \Delta\sigma_0}{2} \left( 1 - 4\frac{r_I^2}{r^2} + 3\frac{r_I^4}{r^4} \right) + \sigma_{10} \\ \sigma_{yy} &= \frac{\Delta\sigma_1 + \Delta\sigma_0}{2} \left( 1 + \frac{r_I^2}{r^2} \right) + \frac{\Delta\sigma_1 - \Delta\sigma_0}{2} \left( 1 + 3\frac{r_I^4}{r^4} \right) + \sigma_{11} \\ \tau_{xy} &= 0 \end{aligned} \quad (3)$$

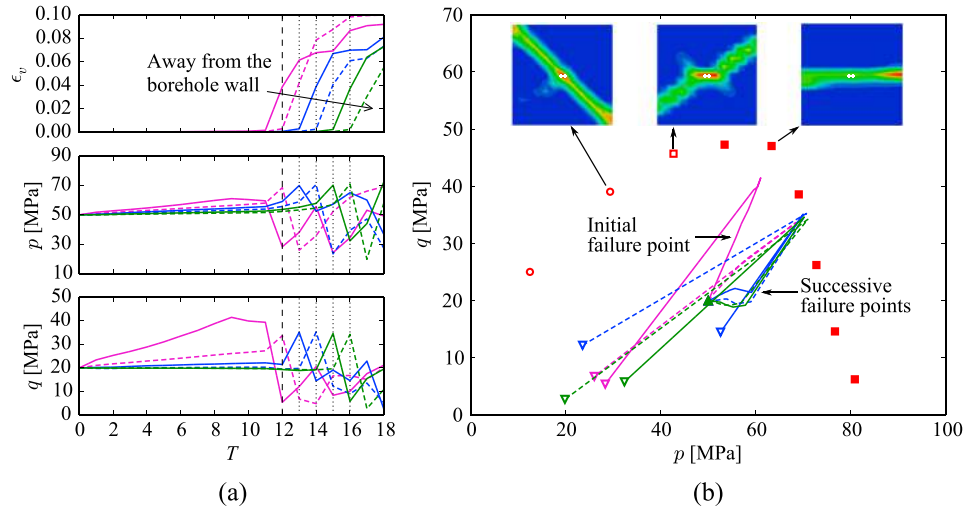


**Figure 10.** (a) The time-sequence evolution of stress concentration for selected six representative volume elements (RVEs; marked as white dots in Figure 9a). The arrow in the top graph shows the relative position of the six RVEs along the  $\sigma_0$  spring line. The dashed vertical line marks the initiation of the compaction bands at  $T = 12$ . The four dotted vertical lines mark the successive failure of the sequential RVEs. (b) Stress paths of the selected six RVEs. The solid upward triangle indicates the starting point of the stress paths, while the open downward triangles indicate the end points. The red markers show the yield stresses obtained from biaxial discrete element method simulations on the RVE at different confining pressures. The different markers indicate the occurrence of varying failure patterns with the increase in confining pressure shown as the insets (open circle for shear band, open square for mixed-mode failure, and solid square for compaction band).

The mean stress  $p$  and the deviatoric stress  $q$  can be derived accordingly:

$$p = \frac{\sigma_x + \sigma_y}{2} = \frac{\sigma_1 + \sigma_0}{2} + \Delta\sigma_1 \times \frac{r_1^2}{l^2} - \Delta\sigma_0 \times \frac{r_1^2}{l^2} \quad (4)$$

$$q = \sigma_y - \sigma_x = (\sigma_1 - \sigma_0) + \Delta\sigma_1 \left( -\frac{r_1^2}{l^2} + \frac{3r_1^4}{l^4} \right) - \Delta\sigma_0 \left( -\frac{3r_1^2}{l^2} + \frac{3r_1^4}{l^4} \right)$$

The influence of the borehole on  $p$  and  $q$  is given by terms of  $l^{-2}$  and  $l^{-4}$ . If Loading Path i (shown in Figure 3) is followed, only  $\sigma_{11}$  is reduced while  $\sigma_{10}$  is unchanged in the early stage. The concentration of  $p$  is caused by  $\Delta\sigma_1 \times \frac{r_1^2}{l^2}$ , which explains the mild decrease of  $p$  along  $\sigma_0$  spring line as shown in Figure 9c, while the concentration of  $q$  is caused by  $\Delta\sigma_1 \left( -\frac{r_1^2}{l^2} + \frac{3r_1^4}{l^4} \right)$ , which explains the rapid decay of  $q$  along  $\sigma_0$  spring line as shown in Figure 9e. For Points A and A' at the borehole wall, the stress components before failure can be calculated according to equation (3) with  $l = r_1$ , leading to  $\sigma_{xx} = \sigma_0$ ,  $\sigma_{yy} = \sigma_1 + 2\Delta\sigma_1$ . Hence, Points A and A' experience exactly a typical biaxial compression (cf. Figure 8b).

By applying biaxial compression on the initial RVE at different confining pressures, the yield stresses for these material points can be obtained, whose locus is plotted in the  $q$ - $p$  plane (shown as red markers in Figure 10b). The three kinds of markers indicate three failure modes (open circle for shear failure, open square for mixed-mode failure, and solid square for compaction failure; see the insets) to occur in biaxial compression depending on the confining pressure. The stress paths of the selected RVEs (marked in Figure 9a) are superimposed in Figure 10b for comparison. It is seen the initial failure point at the borehole wall (close to Point A) undergoes a stress path similar to that in biaxial compression tests until it reaches its peak in the high-mean-stress regime (the purple line in Figure 10b). Due to different decay rates of the concentration of  $p$  and  $q$ , stress paths of successive failure points deviate to the right side, which renders the failure pattern to continue to develop as a compaction band. Figure 10 presents clearly that the stress concentration ahead of the band tip propels the propagation of compaction bands.

### 3.3. Influence of Mean Stress on the Initial Failure Pattern

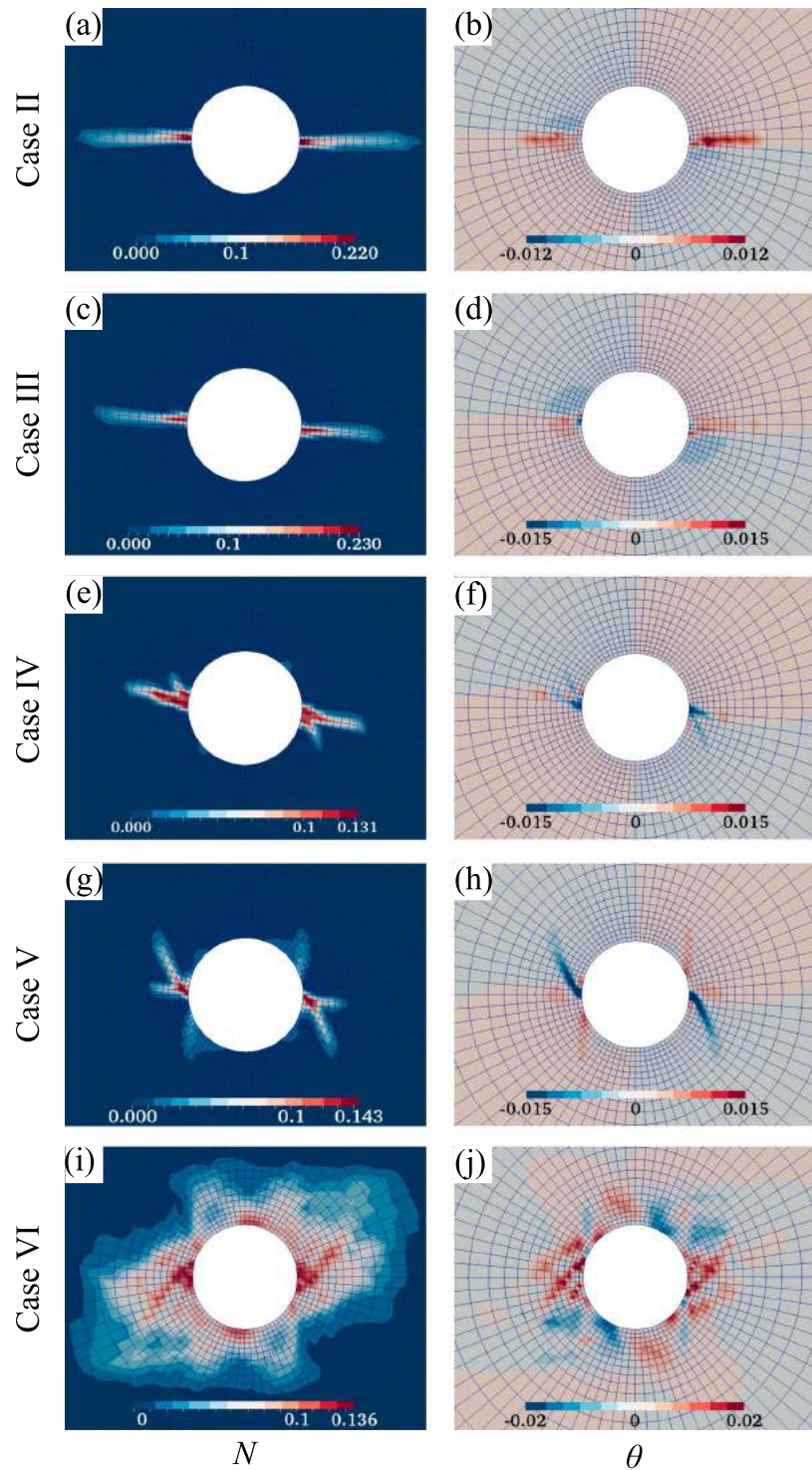
The failure patterns are commonly recorded in laboratory drilling experiments according to the final shapes of the breakouts, but no real-time particle-scale observation is possible. While “fracture-like” breakouts are explained as emptied compaction bands, V-shaped breakouts are considered to be shear or extensile failure (Haimson & Lee, 2004). Meanwhile, the failure pattern is often interpreted as dependent on material property and breakout dimensions on far-field stresses (Haimson, 2007; Haimson & Lee, 2004). However, triaxial compression testing data on high-porosity sandstones indicate that the failure patterns depend crucially on the confining pressure. Shear bands more often occur in the brittle regime of sandstone at relatively low confining pressure, while compaction bands emerge as the confining pressure exceeds the brittle-ductile transition threshold (Charalampidou et al., 2011; Tembe, Baud, & Wong, 2008; Wong, David, & Zhu, 1997). To examine the influence of stress state/loading path on the possible failure patterns, we further explore a number of cases with different far-field stresses and loading paths (see Figure 3 for the loading paths).

Figure 11 shows the mature failure patterns (in terms of  $N$  and  $\theta$ ) for Cases II–VI following the three different global loading paths. The far-field stresses (at the final stage for Case VI) are summarized in Table 2. The failures in the first four cases (Cases II–V) are induced by reducing the support stresses. Figures 11a and 11b show mature compaction bands in terms of  $N$  and  $\theta$  developed in Case II following Path ii with far-field stresses of  $\sigma_0 = 40$  MPa,  $\sigma_1 = 60$  MPa. The pattern resembles that observed in Case I following Path i at the same far-field stresses, in terms of the width and the tilting angle of the band (as shown in the second column of Figure 7). However, far-field stresses alone cannot dictate the failure patterns. Indeed, Figures 11c–11f show the mature failure patterns for two cases with the same far-field stresses of  $\sigma_0 = 30$  MPa,  $\sigma_1 = 45$  MPa but different global loading paths. Clear compaction bands are observed in Case III following Path i, whereas curvilinear shear bands deviating from the  $\sigma_0$  spring line are observed accompanying the compaction bands along the radial direction in Case IV following Path ii. A similar mixed-mode failure showing compaction bands and curvilinear shear bands is found in Case V with far-field stresses of  $\sigma_0 = 20$  MPa,  $\sigma_1 = 35$  MPa following Path i (as shown in Figures 11g and 11h). It is observable that there are intense damage zones near Points A and A' (see Figure 5) and the mild damages farther away from the borehole wall. In experimental tests, these zones may indicate fragmented rocks or flakes which are likely to be removed during/after tests. This could cause possible misinterpretations of the failure mode if only the final profile of the breakout is analyzed.

Figures 11i and 11j show the mature failure pattern of Case VI following Path iii when  $\sigma_0 = 30$  MPa,  $\sigma_1 = 40$  MPa. Initially, when  $\sigma_0$  and  $\sigma_1$  are increased at the same rate, the sandstone is subjected to hydrostatic stress without apparent stress concentration. The failure develops all around the borehole wall without a preferred direction (not presented here). In the second stage when  $\sigma_1$  exceeds  $\sigma_0$ , the degree of failure in terms of  $N$  is intensified along the horizontal direction. A shear failure pattern is identifiable from the observations of the contour of  $N$  in conjunction with that of  $\theta$ , although a clear band is not obvious. The failure is not as localized as in other cases due to the initial hydrostatic loading and may finally lead to V-shaped failure. Indeed, the change of failure pattern from a “fracture-like” breakout to a V-shaped breakout was also reported in experiments when test methods change from drilling into rock mass subjected to preexisting far-field stresses to applying far-field stresses on a specimen with a hole (Haimson, 2003).

Apparently, it is possible that different global loading paths may give rise to different failure patterns, which renders the borehole problem much more complicated to comprehend. Meanwhile, the yield stresses in Figure 10b indicate the alteration in failure mode from shear band to compaction band with the increase in mean stress in biaxial compression. A further comparison of the stress paths in the various cases discussed above may help to elucidate the dependence of failure patterns on the far-field stresses and stress paths. To this end, we plot the local stress paths of the material points near Point A in different cases in Figure 12. The yield stresses of the RVE are also plotted for comparison.

Apparently, the RVEs in cases where Path i is followed (Cases I, III, and V) present similar stress paths as in biaxial compression tests, whereas those in cases following Path ii (Cases II and IV) demonstrate a much steeper stress path due to the reduction in  $\sigma_{10}$  from the very beginning. In other words, starting from the same initial state, the selected RVEs in cases following Path ii fail at a relatively lower mean stress  $p$  than those in cases following Path i. Starting from different initial stress states, the selected RVEs in Cases IV and V undergo different stress paths to converge to a similar failure point as shown in Figure 12, which also partly explains the similar mixed-mode failure patterns shown in the two cases (see Figures 11e and 11g). Similarly, Cases II and



**Figure 11.** Zoomed views of the failure patterns showing the effects of initial stress state and loading path (case II:  $\sigma_0 = 40$  MPa and  $\sigma_1 = 60$  MPa; cases III and IV:  $\sigma_0 = 30$  MPa and  $\sigma_1 = 45$  MPa; case V:  $\sigma_0 = 20$  MPa and  $\sigma_1 = 35$  MPa; case VI:  $\sigma_0 = 30$  MPa and  $\sigma_1 = 45$  MPa [final stage]). Note that cases II and IV follow loading path ii, cases III and V follow loading path i, and case VI follows loading path iii.

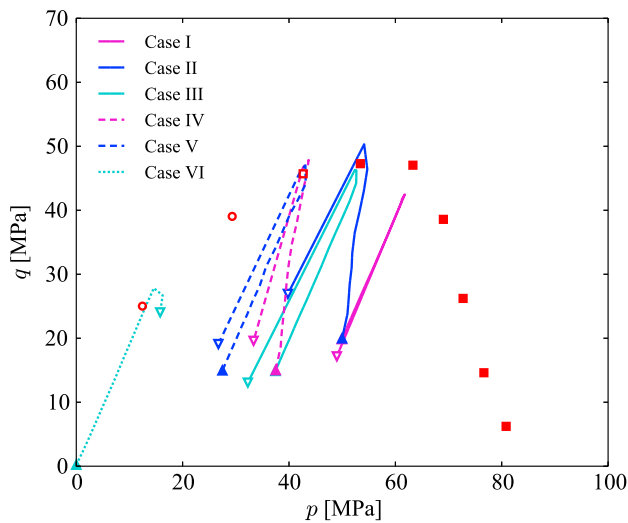


**Figure 12.** Stress paths of the Gauss points close to point A in different cases. Refer to Figure 10b for the meanings of different markers. The solid stress paths indicate the occurrence of compaction band; the dashed stress paths stand for mixed-mode failure; the dotted stress path indicates shear failure.

III reach the same yield state and end up with the same compaction failure pattern (see Figures 11a and 11c). The selected RVE in Case VI undergoes a stress path similar in uniaxial compression tests due to the lack of support stresses during the loading. With rather low mean stress, the failure pattern is shear dominated (see Figure 11i). The dotted, dashed, and solid stress paths indicate the occurrence of shear failure, mixed-mode failure, and compaction band around a borehole respectively. Comparing with the yield stresses of the RVE presenting in different markers, it is interesting to note that mean stress, the controlling factor of failure mode in biaxial compression, dominates the failure pattern around a borehole as well.

### 3.4. The Roles of Material Property

The foregoing discussion has been focused on the effects of stresses to highlight the pressure-dependent nature of sandstones. The roles played by the material property are by no means less important. Indeed, the borehole failure in different rocks may range from V-shaped breakouts formed by extensile cracking parallel to the  $\sigma_1$  direction in granites and V-shaped breakouts formed by dilatant shear cracks in Cordova Cream to “fracture-like” breakouts developed in quartz-rich high-porosity sandstones (Haimson, 2001, 2007; Haimson & Klaetsch, 2007; Haimson & Song, 1993; M. Lee & Haimson, 1993).

“Fracture-like” breakouts have been reported in high-porosity sandstones and are considered to be analogous to compaction bands. Laboratory drilling experiments on three kinds of Berea sandstones (BSs25, porosity: 25%; BSs22, porosity: 22.5%; BSs17, porosity: 17%) indicate that BSs17 exhibits V-shaped breakouts which distinguish from the “fracture-like” breakouts developed in BSs22 and BSs25 (Haimson, 2001, 2003). However, the V-shaped breakouts developed in Tablerock sandstone (porosity: 28 %  $\pm$  3%), attributable to the stronger cementation by microcrystalline quartz, suggest that the dominating factor is cohesion strength rather than porosity (Haimson & Lee, 2004). It is noted that the much stronger BSs17 was cemented by iron rich clay, while BSs22 and BSs25 were cemented by sutured contacts (Haimson, 2003). Bessinger et al. (1997) have conducted uniaxial compression on sintered glass bead bricks with different degrees of sintering. They found conical-shaped breakouts in bricks with a high degree of sintering, and “fracture-like” breakouts along direction perpendicular to the compressive stress in bricks with a lower degree of sintering. The hierarchical coupling feature of the multiscale approach adopted in this study facilitates direct linking of the microparameters with the macrobehavior. The porosity and the cohesion strength have widely been considered important properties of sandstones whose roles will be carefully investigated here.

#### 3.4.1. Porosity

To investigate the separate effects of porosity, we show in Figure 13 the initiation and the final stage of Case XII with a low-porosity specimen ( $n = 0.279$ ). Other setups, including the initial stress state, the loading path, and the cohesion strength  $c$ , are kept the same as Case I, in which compaction bands are observed. As shown in Figures 13a–13d at  $T = 30$ , a set of shear bands are initiated from the borehole wall close to the  $\sigma_0$  spring line at around  $\alpha = 5^\circ$  and  $\alpha = -175^\circ$  (refer to Figure 5 for  $\alpha$ ). Meanwhile, another set of localized zones incepts at around  $\alpha = -15^\circ$  and  $\alpha = 165^\circ$ , serving as an origin for more shear bands. The areas near Points A and A' are left largely undamaged surrounded by the two sets of localized failure zones till the final stage (see Figure 13e). With the decreasing support stresses, the initial shear bands propagate while further new shear bands are initiated from the borehole wall, forming a two-way crossed curvilinear final pattern at  $T = 48$  as in Figures 13e–13h. From the contour of rotation (see Figure 13f), the two sets of conjugate curvilinear shear bands have distinct rotation directions. The multiple arrays of shear bands with largely undamaged interlayers result in a wider angle for the V-shaped pattern. Indeed, largely intact fragments spalling from the borehole wall due to shear cracks have been reported in the observation of V-shaped breakouts in sandstones (Ewy & Cook, 1990b; Haimson, 2007).

The distinct failure patterns in Cases XII and I highlight high porosity as a favorable factor for compaction bands. The stress path of the RVE near Point A in Case XII is further illustrated as the dotted blue line in Figure 14. The empty blue circles depict the yield stresses of the low-porosity RVE, showing a linear yield

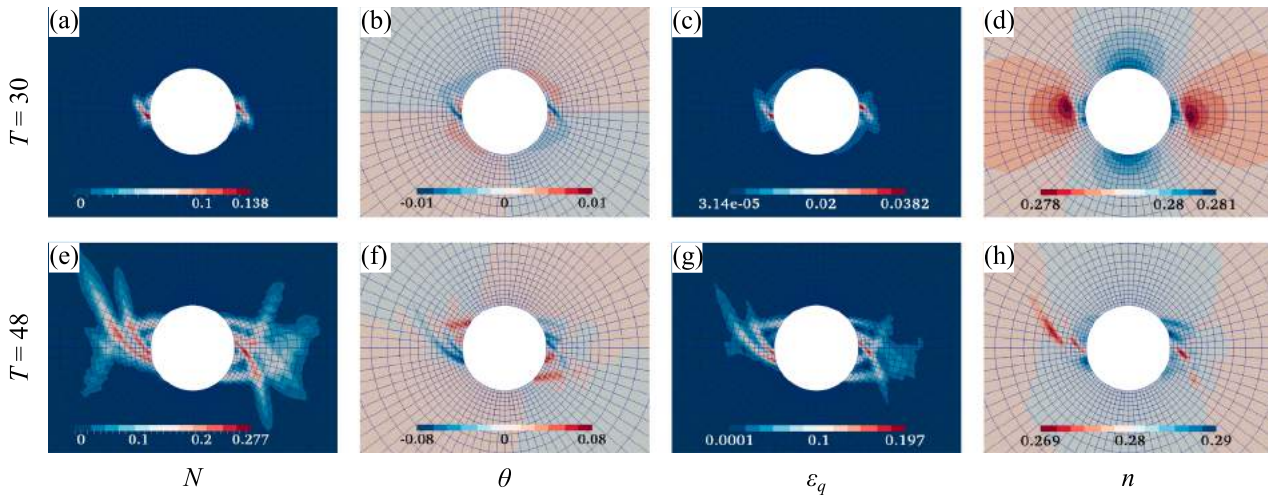


**Figure 13.** Zoomed views of the initiation and final failure patterns of the low-porosity specimen (case XII,  $\sigma_0 = 40$  MPa and  $\sigma_1 = 60$  MPa). The support stresses  $\sigma_{i0}$  and  $\sigma_{i1}$  are reduced following loading path i.

locus (Mohr-Coulomb type failure). The stress path and the yield locus suggest that the failure pattern in Case XII can be regarded as a brittle shear failure as illustrated in Figure 13. The stress path of the selected Gauss point in Case I and its corresponding yield stresses are plotted in red for comparison, which shows a compaction failure as shown in Figure 7.

### 3.4.2. Cohesion Strength

The influence of cohesion strength  $c$  on the failure patterns is examined by conducting simulations on specimens with the same structure. Figure 15 shows the variation of failure patterns with different cohesion strength (for Cases X, VII, and XI, respectively). Figures 15a and 15b present the mixed-mode failure of Case X with  $c = 9.0$  GPa at  $\sigma_0 = 30$  MPa,  $\sigma_1 = 45$  MPa, where straight compaction bands and curvilinear shear bands initiate near Points A and A'. In comparison, Case III shows clear compaction bands in Figures 11c and 11d due to a slightly smaller cohesion of 6.8 GPa with the same far-field stresses and loading path. Cases VII and XI have the same far-field stresses ( $\sigma_0 = 20$  MPa,  $\sigma_1 = 30$  MPa) and follow the same Loading Path i. With  $c = 4.5$  GPa, Case XI presents clear compaction bands along the radial direction in conjunction with curvilinear shear bands in Figures 15e and 15f. But with a slightly larger cohesion of 6.8 GPa, Case VII shows only shear bands in Figures 15c and 15d. These results show that a specimen with a lower cohesion strength has a higher potential to develop compaction bands, which confirms the speculation by Haimson and Lee (2004) according to their comparison between Tablerock sandstone and Mansfield sandstone.

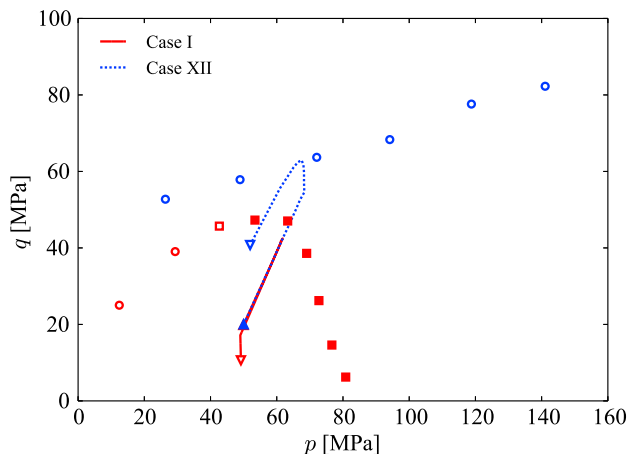


**Figure 14.** Stress path of the selected Gauss point in case XII and the corresponding yield stresses for low-porosity representative volume element (blue open circles). The high-porosity case at the same initial stress state (cases I) and its corresponding yield stresses are plotted in red for comparison. Refer to Figure 10b for the meanings of different markers.

The stress paths of the Gauss points near Point A in these cases are illustrated in Figure 16 to help interpret the effect of  $c$ . The isolate markers illustrate the yield stresses of the RVEs for these cases. Evidently, the increase in  $c$  leads to the expansion of the yield locus as well as an apparent shift of the failure mode regime. With increasing  $c$ , a higher mean stress is needed to convert from shear failure to mixed-mode failure or from mixed-mode failure to compaction failure. In Cases VII and X, the selected Gauss points follow the stress paths similar to biaxial compression tests during the early stage with constant  $\sigma_{i0}$ , then the stress paths turn to vertical lines due to the decrease in  $\sigma_{i0}$ . Hence, the selected RVEs in Cases VII and X fail at the same mean stress with their counterparts of lower  $c$ , Cases XI and III, respectively. However, the failure mode converts from compaction failure in Case III to mixed-mode failure in Case X and from mixed-mode failure in Case XI to shear failure in Case VII due to the increase in cohesion strength.

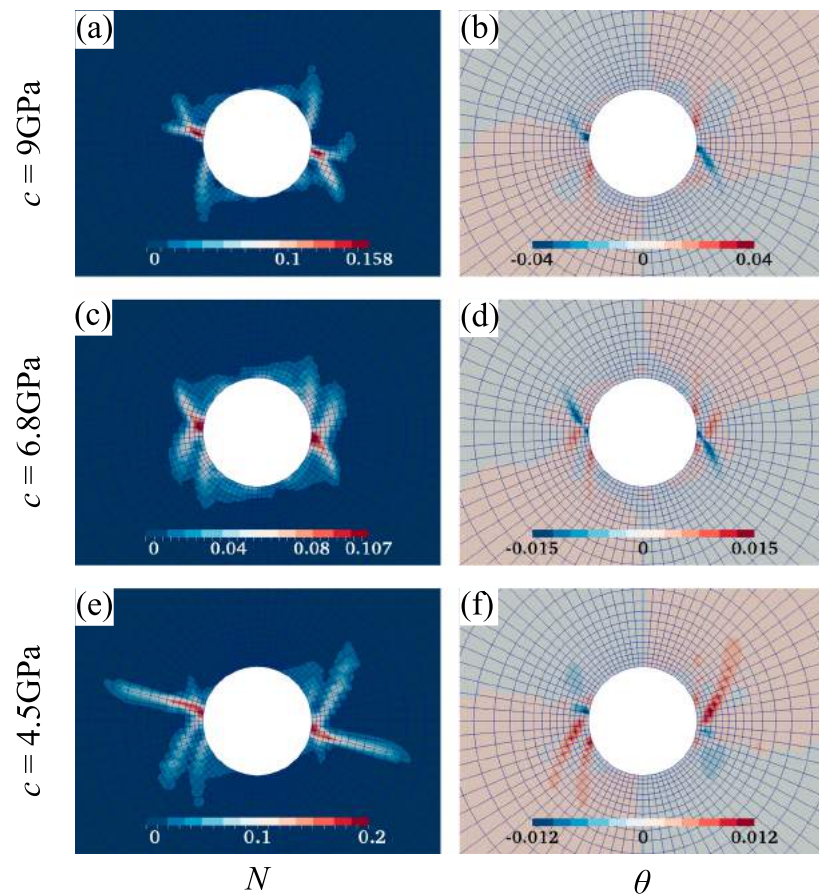


**Figure 15.** Zoomed views of the failure patterns showing the effect of cohesion strength [(a and b), case X:  $\sigma_0 = 30$  MPa and  $\sigma_1 = 45$  MPa; [c and d], case VII:  $\sigma_0 = 20$  MPa and  $\sigma_1 = 30$  MPa; [e and f], case XI:  $\sigma_0 = 20$  MPa and  $\sigma_1 = 30$  MPa). The support stresses  $\sigma_{i0}$  and  $\sigma_{i1}$  are reduced following loading path i.

#### 4. Correlation Between Size and Orientation of Borehole Failure and the Far-Field Stresses

The size and orientation of the breakouts can be useful for identifying the tectonic stress state. The breakout direction has been widely used as a confident indicator for the direction of the minimum horizontal stress. Indeed, about 19% of the stress orientations in the World Stress Map database were determined based on borehole breakouts (Reinecker, Tingay, & Müller, 2003). However, the attempt to determine the magnitude of the in situ stresses based solely on breakout size must be treated with caution (Ljunggren et al., 2003). While the breakout dimensions in well-controlled laboratory drilling experiments have been found to correlate strongly with the far-field stresses (Haimson & Lee, 2004), they may meanwhile be affected by the stress path, the properties of drilling fluid, the drill-bit penetration rate, and the borehole size (Ewy & Cook, 1990b; Sheets & Haimson, 2004; Zheng et al., 1989). The following section is devoted to examining the correlated factors that affect the size and orientation of borehole failure.

Notably, however, the breakout dimension in experiments is commonly identified after the removal of rock flakes. Since no removal mechanism is modeled in the current simulation, we choose the contour of  $N$  corroborated with other quantities including  $n$ ,  $\epsilon_{qi}$ ,  $\epsilon_{vi}$ , and  $\theta$  for this purpose. This analogy may deviate from the breakout dimensions measured in experiments or real boreholes. In section 3.3, the effect of loading path on the failure pattern has been thoroughly discussed. The dimension of the borehole failure in the following subsections will then be compared among the cases following Loading Path i. The contours of  $N$  at the final stage in all the cases are employed for the comparison.

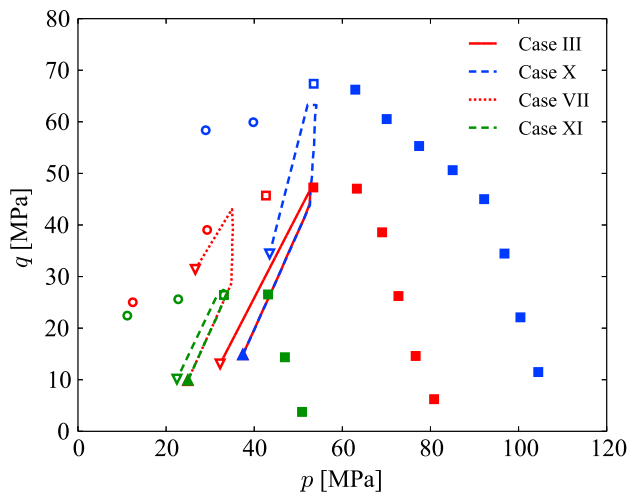


**Figure 16.** Stress paths of the selected Gauss points near point A in different cases. The isolate markers (open circles, open squares, solid squares, see Figure 10b for their meanings) illustrate the yield stresses of the representative volume elements with different  $c$ . Color interpretation: green for  $c = 4.5$  GPa, red for  $c = 6.8$  GPa, and blue for  $c = 9.0$  GPa. The line style of the stress path indicates the failure mode in corresponding cases (see Figure 12 for their meanings).

tip. Figure 17c shows the final pattern for Case VII where  $\sigma_0 = 20$  MPa and  $\sigma_1 = 30$  MPa. Clear curvilinear shear bands instead of compaction bands can be observed initiating from Points A and A' (see a zoomed view in Figure 15c).

The above comparison indicates that if  $\sigma_1/\sigma_0$  is kept a constant, a decrease in  $\sigma_0$  will lead to decreased failure depth (along the radial direction), failure area, and debonding number  $N$ . Moreover, the mature failure pattern can vary from a compaction band to a shear band with the decrease in  $\sigma_0$ .

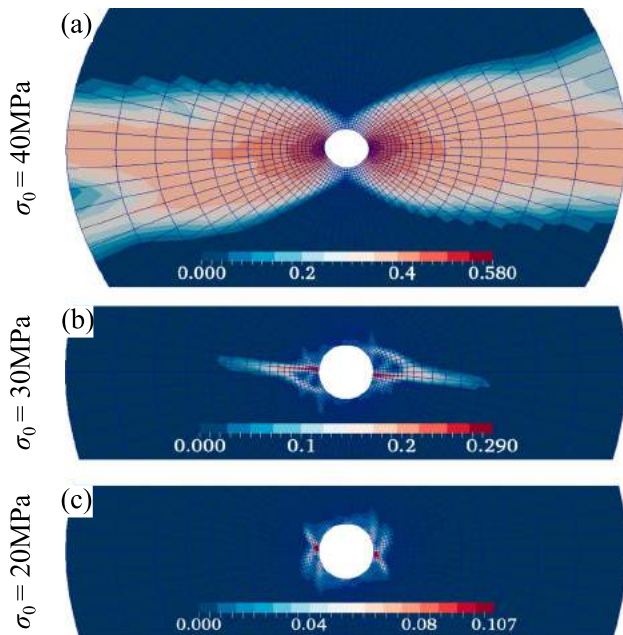


**Figure 17.** Zoomed views of final failure patterns in terms of  $N$  showing the effect of  $\sigma_0$ . (a) Case I; (b) Case III; (c) Case VII. All three cases are subjected to the same far-field stress ratio  $\sigma_1/\sigma_0 = 1.5$ . The support stresses  $\sigma_{10}$  and  $\sigma_{11}$  are reduced following loading path i.

#### 4.1. The Influence of $\sigma_0$

To investigate the influence of  $\sigma_0$ , we have compared Cases I, III, and VII at the same far-field stress ratio  $\sigma_1/\sigma_0 = 1.5$ . The final failure patterns in terms of  $N$  are illustrated in Figure 17. In Case I where  $\sigma_0 = 40$  MPa, the failure pattern is a typical compaction band as introduced in section 3.1. The bandwidth begins to increase from  $T = 16$  when  $\sigma_{10} = \sigma_{11} = 40$  MPa. The final pattern displays a rather wide compaction band as shown in Figure 17a. The thickening in width of the compaction band is caused by the hardening of the compacted region. A similar spreading pattern of compaction bands was also observed in laboratory triaxial compression tests where it was named as “compaction front” (Baud, Klein, & Wong, 2004; Olsson, Holcomb, & Rudnicki, 2002). Since the deformation band exceeds the lateral boundaries of the domain, it is irrelevant to determine the exact length.

Figure 17b presents the final failure pattern of Case III where  $\sigma_0 = 30$  MPa and  $\sigma_1 = 45$  MPa. The failure pattern features a narrow, straight compaction band forming along the direction of  $\alpha \approx -5^\circ$  entangled by several curvilinear shear bands. Likewise in Case I, the compaction failure also initiates from Points A and A' in this case and then penetrates into the farther rock (see Figure 11c). However, with further reduction in support stresses, shear failures emerge from the borehole wall and propagate curvilinearly into the host rock to merge with the compaction bands at the corresponding

#### 4.2. The Influence of Far-Field Stress Ratio $\sigma_1/\sigma_0$

The influence of far-field stress ratio on the failure patterns has been examined with Cases VII, V, and VIII at the same  $\sigma_0 = 20$  MPa as presented in Figure 18. With the increase in  $\sigma_1$  from 30 to 35 MPa (for Cases VII and V), the extending length of the shear bands increases apparently, and two short compaction bands are formed from Points A and A' along the direction of  $\alpha \approx -5^\circ$  and  $175^\circ$ . When  $\sigma_1$  further increases to 40 MPa in Case VIII, the failure pattern is more compaction dominated. Two longer compaction bands are formed along  $\sigma_0$  spring line in conjunction with curvilinear shear bands deviating from  $\sigma_0$  spring line. Moreover, the angle between the compaction band and  $\sigma_0$  spring line decreases due to the increased  $\sigma_1$ . The transition from the shear failure in Case VII to mixed-mode failure in Cases V and VIII is due to the increase in mean stress, which is consistent with the interpretation in section 3.3. The investigations in sections 4.1 and 4.2 indicate the increase in failure depth, failure area, and damage extent with increased stress ratio  $\sigma_1/\sigma_0$  or minor principal stress  $\sigma_0$ , an observation consistent with well-controlled drilling experimental results (Haimson & Kovachik, 2003; Haimson & Lee, 2004).

#### 4.3. Borehole Failure Under Hydrostatic Far-Field Stress

The breakout orientation has been widely used as an indicator for the minor principal stress direction. Our previous simulations show that the

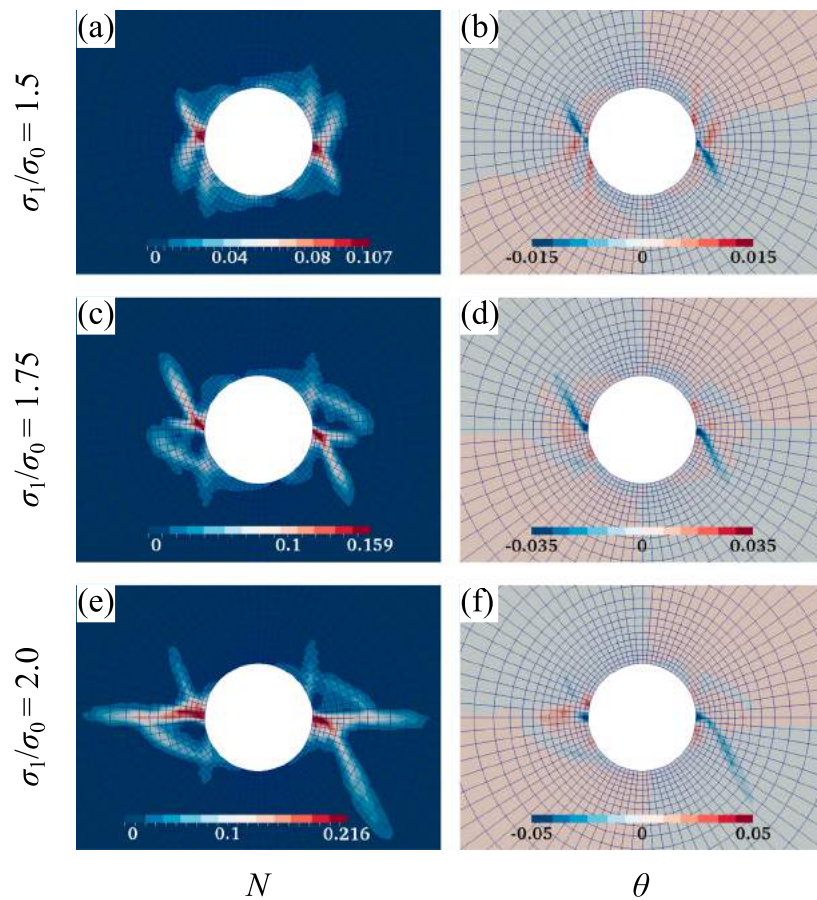


**Figure 18.** Zoomed views of the final failure patterns in terms of  $N$  and  $\theta$  showing the effect of stress ratio  $\sigma_1/\sigma_0$ . (a and b) Case VII; (c and d) Case V; (e and f) Case VIII. All three cases share the same  $\sigma_0 = 20$  MPa. The support stresses  $\sigma_{10}$  and  $\sigma_{11}$  are reduced following loading path i.

failure initiates from Points A and A' and develops near the  $\sigma_0$  direction when the inner stresses are reduced. As reported in laboratory experiments, diametrically opposite breakouts may also develop under hydrostatic stress due possibly to the strength anisotropy of the specimen (Cuss et al., 2003; Ewy & Cook, 1990b).

To examine the correlation between the breakout orientation and the far-field stress direction, we have investigated Case IX with an initial hydrostatic stress state of  $\sigma_1 = \sigma_0 = 40$  MPa. Figures 19a–19d illustrate the initiation of the shear failure at  $\sigma_{11} = \sigma_{10} = 12.5$  MPa. The failure occurs around the borehole without an apparently preferred direction, indicating a largely isotropic condition for the material. Nevertheless, it is noticed that the shear band initiating from the direction of  $\alpha \approx 40^\circ$  develops slightly more intensely than others, which may have been caused by the mild anisotropy in the initial RVE. With further reduction in inner support stresses, the shear bands proceed to penetrate into the host rock. Two sets of conjugate shear bands can be easily identified from the contour of  $\theta$  as shown in Figure 19f. The contour of volumetric strain  $\epsilon_v$  (where contraction is taken as positive) as shown in Figure 19h suggests certain dilation near the borehole wall. This may cause the rock flakes to spall and be separated from the host rock, which is consistent with the observation of separated fragments from the host rock caused by cracks in Tablerock sandstone (Haimson, 2007). Note the diametrically opposite failure pattern shown in Figures 19e–19h, which confirms the possibility of diametrically opposite breakouts at hydrostatic stress state. The break of radial/axial symmetry in deformation under symmetric boundary condition due to material anisotropy has also been discussed in Guo, Zhao, and Sun (2016) and Zhao and Guo (2015).

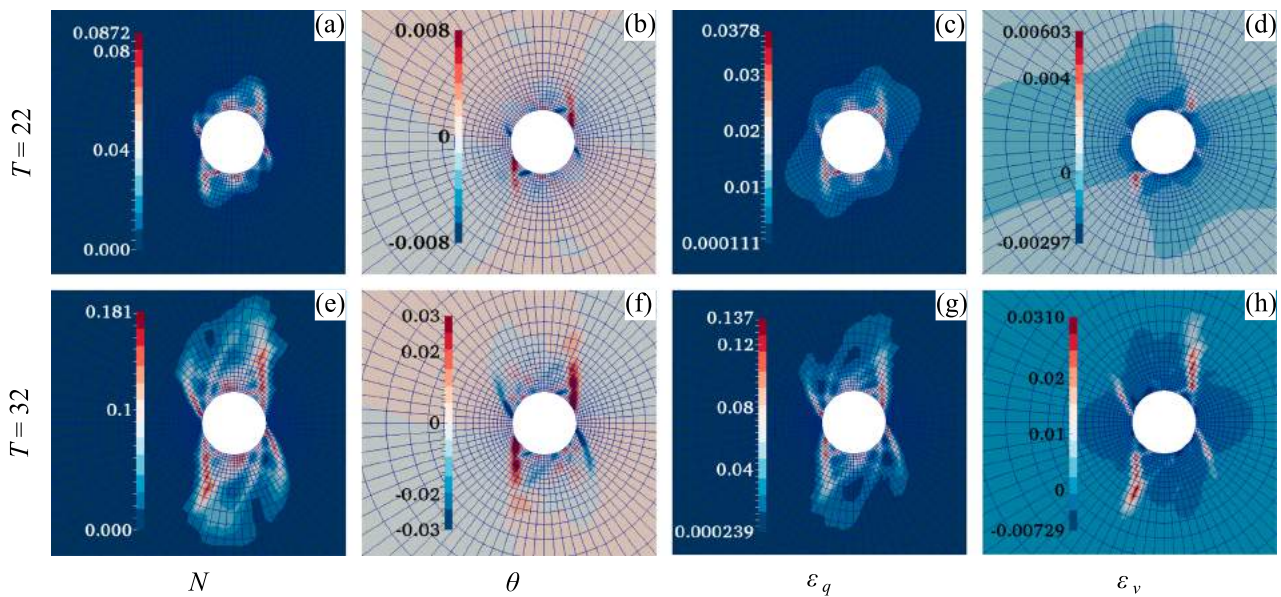


**Figure 19.** The zoomed views of (a–d) the initiation and (e–h) the final stage of the failure for case IX in terms of  $N$ ,  $\theta$ ,  $\epsilon_q$ ,  $\epsilon_v$  ( $\sigma_1 = \sigma_0 = 40$  MPa). The support stresses  $\sigma_{j0}$  and  $\sigma_{j1}$  are reduced following loading path  $i$ .

## 5. Conclusions

A multiscale investigation on the borehole instabilities in high-porosity sandstones has been presented. We employed a hierarchically coupled FEM/DEM approach wherein the DEM solution to a granular assembly as RVE is computed at each integration point to provide required material response for the FEM to avoid phenomenological constitutive assumptions. RVEs with high-porosity structure were used to reproduce the typical mechanical response of high-porosity sandstones. The typical progressive failure of a borehole is simulated by gradually reducing the inner support stresses or increasing the far-field stresses. We demonstrated that the multiscale simulations can well capture the onset and development of a wide variety of failure patterns around the borehole, including compaction bands (“slot-like” breakout), mixed-mode failure, and shear failure. Four microstructurally extracted quantities, the normalized debonding number, the porosity, the deviatoric strain, and the averaged particle rotation, offer corroborated, consistent identifications of the failure patterns. The formation of failure patterns was found depending crucially on the loading path, the stress state, and material properties including porosity and cohesion strength. The major findings from this study are summarized below:

1. The compaction bands around a borehole initiate at or near the intersection points of the  $\sigma_0$  spring line and the borehole wall due to stress concentration. The interparticle debonding and pore collapse in the bands lead to stress relaxation and the propagation of the stress concentration to the band tips, which further propels their penetration into the host rock. Further decrease in the inner support stresses may lead to the thickening of the bands and the shear-dominated failure near the borehole wall.
2. A variety of failure patterns around a borehole have been captured with different initial stress states and global loading paths. The comparison of the stress paths of the initial failure points in different cases reveals that the failure pattern around a borehole may change from shear failure to mixed-mode failure to compaction failure with the increase in mean stress.
3. The decrease in porosity results in a positively sloped linear yield locus on the  $q$ - $p$  plane within the stress range of interest. Thus, by changing the high-porosity specimen to a low-porosity one, the failure mode shifts from clear compaction bands to multiple arrays of shear bands with largely undamaged interlayers. The increase in cohesion strength expands the yield locus and enlarges the critical mean stress between different failure patterns. Hence, under the same far-field stresses and following the same loading path, the failure mode may change from compaction failure to mixed-mode failure or from mixed-mode failure to shear failure due to the increase in cohesion strength.

- The sensitivity of the size and the orientation of the failure to far-field stresses have been analyzed with simulations following the same loading path. The qualitative comparison of the final stage (when  $\sigma_{10} = \sigma_{11} = 0$ ) of two sets of cases with varied minor principal stress  $\sigma_0$  or stress ratio  $\sigma_1/\sigma_0$  illustrates clearly the increase in the failure depth and area and the damage extent with the increase in  $\sigma_0$  or  $\sigma_1/\sigma_0$ . The diametrically opposite failure patterns are usually indicators for the minor principal stress direction. However, they may also take place under hydrostatic far-field stress when material anisotropy is present.

The current study can be further extended toward more realistic modeling of the borehole problem in the future. First, the borehole has been simplified as a 2-D ring problem, which definitely needs to be further extended to a full 3-D analysis to fully consider the complicated tectonic stress, the stress concentration at the bottom of the borehole (Schmitt et al., 2012), and sometimes highly heterogeneous and anisotropic sandstone around a borehole. In this regard, a recent 3-D multiscale modeling study can be used as a good reference (Guo & Zhao, 2016a). Second, the microstructure of real sandstone can be so complicated that it cannot be represented by an overly simplified RVE with simple bonded contact model and high-porosity structure as introduced in the study. A more rigorous method is to reconstruct sandstone microstructures based on and calibrated by data obtained by advanced testing techniques such as synchrotron X-ray tomography (Andò et al., 2012). Third, the study has focused on such microscopic mechanisms as pore collapse and bond breakage but has excluded the possibility of grain crushing which has indeed been observed in some borehole breakouts. While it is challenging, grain crushing can constitute a key failure mechanism (Haimson, 2007) and should be incorporated in borehole modeling in the future. Last, most engineering problems pertinent to the formation of borehole are saturated or partially saturated, whereby the effect of pore fluid is important. A fully coupled hydromechanical analysis may appear to be more relevant in these cases and will be further considered. In this regard, a recent development of our multiscale modeling approach on cross-scale hydromechanical modeling can serve as a good reference (Guo & Zhao, 2016b; see also Wang & Sun, 2016).

#### Acknowledgments

The authors wish to thank Prof. Jacques Desrues, the Associate Editor Prof. Douglas Schmitt, and the other anonymous reviewer for their constructive comments on the manuscript. The study has been financially supported by the National Natural Science Foundation of China under project 51679207 and the Research Grants Council of Hong Kong through GRF project 16210017. N.G. is supported by a Discovery Grant from the Natural Sciences and Engineering Research Council of Canada. Data used to create the figures presented in this article are available at the following link: <https://figshare.com/s/f24b06ddeb3924-d6a87c>. All figures were generated by the open-source data analysis and visualization application Paraview (<https://www.paraview.org>). The software code used for modeling and generating the data in this study has been based on the open-source parallel hierarchical multiscale modeling code FEM × DEM accessible via YADE (<https://yade-dem.org/doc/FEMxDEM.html>).

#### References

- Al-Ajmi, A. M., & Zimmerman, R. W. (2006). Stability analysis of vertical boreholes using the Mogi-Coulomb failure criterion. *International Journal of Rock Mechanics and Mining Sciences*, 43(8), 1200–1211. <https://doi.org/10.1016/j.ijrmms.2006.04.001>
- Al-Busaidi, A., Hazzard, J. F., & Young, R. P. (2005). Distinct element modeling of hydraulically fractured Lac du Bonnet granite. *Journal of Geophysical Research*, 110, B06302. <https://doi.org/10.1029/2004JB003297>
- Andò, E., Hall, S. A., Viggiani, G., Desrues, J., & Bésuelle, P. (2012). Grain-scale experimental investigation of localised deformation in sand: A discrete particle tracking approach. *Acta Geotechnica*, 7(1), 1–13. <https://doi.org/10.1007/s11440-011-0151-6>
- Andrade, J. E., Avila, C. F., Hall, S. A., Lenoir, N., & Viggiani, G. (2011). Multiscale modeling and characterization of granular matter: From grain kinematics to continuum mechanics. *Journal of the Mechanics and Physics of Solids*, 59(2), 237–250. <https://doi.org/10.1016/j.jmps.202010.10.009>
- Aydin, A., & Ahmadv, R. (2009). Bed-parallel compaction bands in aeolian sandstone: Their identification, characterization and implications. *Tectonophysics*, 479(3–4), 277–284. <https://doi.org/10.1016/j.tecto.2009.08.033>
- Baud, P., Klein, E., & Wong, T.-F. (2004). Compaction localization in porous sandstones: Spatial evolution of damage and acoustic emission activity. *Journal of Structural Geology*, 26(4), 603–624. <https://doi.org/10.1016/j.jsg.2003.09.002>
- Baud, P., Reuschlé, T., Ji, Y., Cheung, C. S. N., & Wong, T.-F. (2015). Mechanical compaction and strain localization in Bleurswiller sandstone. *Journal of Geophysical Research: Solid Earth*, 120, 6501–6522. <https://doi.org/10.1002/2015JB012192>
- Bessinger, B. A., Liu, Z., Cook, N. G. W., & Myer, L. R. (1997). A new fracturing mechanism for granular media. *Geophysical Research Letters*, 24(21), 2605–2608. <https://doi.org/10.1029/97GL02740>
- Bradley, W. B. (1979). Failure of inclined boreholes. *Journal of Energy Resources Technology*, 101(4), 232. <https://doi.org/10.1115/1.3446925>
- Charalampidou, E. M., Hall, S. A., Stanchits, S., Lewis, H., & Viggiani, G. (2011). Characterization of shear and compaction bands in a porous sandstone deformed under triaxial compression. *Tectonophysics*, 503(1–2), 8–17. <https://doi.org/10.1016/j.tecto.2010.09.032>
- Charalampidou, E. M., Hall, S. A., Stanchits, S., Viggiani, G., & Lewis, H. (2014). Shear-enhanced compaction band identification at the laboratory scale using acoustic and full-field methods. *International Journal of Rock Mechanics and Mining Sciences*, 67, 240–252. <https://doi.org/10.1016/j.ijrmms.2013.05.006>
- Crook, T., Willson, S., Yu, J. G., & Owen, R. (2003). Computational modelling of the localized deformation associated with borehole breakout in quasi-brittle materials. *Journal of Petroleum Science and Engineering*, 38(3–4), 177–186. [https://doi.org/10.1016/S0920-4105\(03\)00031-7](https://doi.org/10.1016/S0920-4105(03)00031-7)
- Cui, L., Cheng, A. H. D., Kaliakin, V. N., Abousleiman, Y., & Roegiers, J.-C. C. (1996). Finite element analyses of anisotropic poroelasticity: A generalized Mandel's problem and an inclined borehole problem. *International Journal for Numerical and Analytical Methods in Geomechanics*, 20(6), 381–401. [https://doi.org/10.1002/\(SICI\)1096-9853\(199606\)20:6%3C381::AID-NAG826%3E3.0.CO;2-Y](https://doi.org/10.1002/(SICI)1096-9853(199606)20:6%3C381::AID-NAG826%3E3.0.CO;2-Y)
- Cui, L., Kaliakin, V. N., Abousleiman, Y., & Cheng, A. H. D. (1997). Finite element formulation and application of poroelastic generalized plane strain problems. *International Journal of Rock Mechanics and Mining Sciences*, 34(6), 953–962. [https://doi.org/10.1016/S1365-1609\(97\)80005-6](https://doi.org/10.1016/S1365-1609(97)80005-6)
- Cuss, R. J., Rutter, E. H., & Holloway, R. F. (2003). Experimental observations of the mechanics of borehole failure in porous sandstone. *International Journal of Rock Mechanics and Mining Sciences*, 40(5), 747–761. [https://doi.org/10.1016/S1365-1609\(03\)00068-6](https://doi.org/10.1016/S1365-1609(03)00068-6)
- Desrues, J., Nguyen, T. K., Combe, G., & Caillerie, D. (2015). FEM × DEM multi-scale analysis of boundary value problems involving strain localization. In K. T. Chau & J. D. Zhao (Eds.), *Bifurcation and Degradation of Geomaterials in the New Millennium*. Springer Series in Geomechanics and Geoengineering (pp. 259–265). Berlin: Springer. [https://doi.org/10.1007/978-3-319-13506-9\\_37](https://doi.org/10.1007/978-3-319-13506-9_37)

- Detournay, E., & Cheng, A. H. D. (1988). Poroelastic response of a borehole in a non-hydrostatic stress field. *International Journal of Rock Mechanics and Mining Sciences*, 25(3), 171–182. [https://doi.org/10.1016/0148-9062\(88\)92299-1](https://doi.org/10.1016/0148-9062(88)92299-1)
- Dresen, G., Stanchits, S., & Rybacki, E. (2010). Borehole breakout evolution through acoustic emission location analysis. *International Journal of Rock Mechanics and Mining Sciences*, 47(3), 426–435. <https://doi.org/10.1016/j.ijrmmms.2009.12.010>
- Duan, K., & Kwok, C. Y. (2016). Evolution of stress-induced borehole breakout in inherently anisotropic rock: Insights from discrete element modeling. *Journal of Geophysical Research: Solid Earth*, 121, 2361–2381. <https://doi.org/10.1002/2015JB012676>
- Ewy, R. T. (1993). Yield and closure of directional and horizontal wells. *International Journal of Rock Mechanics and Mining Sciences*, 30(7), 1061–1067. [https://doi.org/10.1016/0148-9062\(93\)90072-L](https://doi.org/10.1016/0148-9062(93)90072-L)
- Ewy, R. T., & Cook, N. G. W. (1990a). Deformation and fracture around cylindrical openings in rock—I. Observations and analysis of deformations. *International Journal of Rock Mechanics and Mining Sciences*, 27(5), 387–407. [https://doi.org/10.1016/0148-9062\(90\)92713-O](https://doi.org/10.1016/0148-9062(90)92713-O)
- Ewy, R. T., & Cook, N. G. W. (1990b). Deformation and fracture around cylindrical openings in rock—II. Initiation, growth and interaction of fractures. *International Journal of Rock Mechanics and Mining Sciences*, 27(5), 409–427. [https://doi.org/10.1016/0148-9062\(90\)92714-P](https://doi.org/10.1016/0148-9062(90)92714-P)
- Fakhimi, A., Carvalho, F., Ishida, T., & Labuz, J. F. (2002). Simulation of failure around a circular opening in rock. *International Journal of Rock Mechanics and Mining Sciences*, 39(4), 507–515. [https://doi.org/10.1016/S1365-1609\(02\)00041-2](https://doi.org/10.1016/S1365-1609(02)00041-2)
- Fjær, E., Holt, R. M., Horsrud, P., Raaen, A. M., & Risnes, R. (2008). *Petroleum related rock mechanics* (2nd ed.). Oxford, UK: Elsevier.
- Francois, B., Labiouse, V., Dizier, A., Marinelli, F., Charlier, R., Collin, F. F. F., et al. (2014). Hollow cylinder tests on boom clay: Modelling of strain localization in the anisotropic excavation damaged zone. *Rock Mechanics and Rock Engineering*, 47(1), 71–86. <https://doi.org/10.1007/s00603-012-0348-5>
- Gelet, R., Loret, B., & Khalili, N. (2012). Borehole stability analysis in a thermoporoelastic dual-porosity medium. *International Journal of Rock Mechanics and Mining Sciences*, 50, 65–76. <https://doi.org/10.1016/j.ijrmmms.2011.12.003>
- Germanovich, L. N., & Dyskin, A. V. (2000). Fracture mechanisms and instability of openings in compression. *International Journal of Rock Mechanics and Mining Sciences*, 37(1–2), 263–284. [https://doi.org/10.1016/S1365-1609\(99\)00105-7](https://doi.org/10.1016/S1365-1609(99)00105-7)
- Guo, N., & Zhao, J. (2013). The signature of shear-induced anisotropy in granular media. *Computers and Geotechnics*, 47, 1–15. <https://doi.org/10.1016/j.compgeo.2012.07.002>
- Guo, N., & Zhao, J. (2014). A coupled FEM/DEM approach for hierarchical multiscale modelling of granular media. *International Journal for Numerical Methods in Engineering*, 99(11), 789–818. <https://doi.org/10.1002/nme.4702>
- Guo, N., & Zhao, J. (2016a). 3D multiscale modeling of strain localization in granular media. *Computers and Geotechnics*, 80, 360–372. <https://doi.org/10.1016/j.compgeo.2016.01.020>
- Guo, N., & Zhao, J. (2016b). Parallel hierarchical multiscale modelling of hydro-mechanical problems for saturated granular soils. *Computer Methods in Applied Mechanics and Engineering*, 305(9), 37–61. <https://doi.org/10.1016/j.cma.2016.03.004>
- Guo, N., Zhao, J., & Sun, W. (2016). Multiscale analysis of shear failure of thick-walled hollow cylinder in dry sand. *Géotechnique Letters*, 6(1), 77–82. <https://doi.org/10.1680/jgele.15.00149>
- Haimson, B. C. (2001). Fracture-like borehole breakouts in high-porosity sandstone: Are they caused by compaction bands? *Physics and Chemistry of the Earth, Part A: Solid Earth and Geodesy*, 26(1–2), 15–20. [https://doi.org/10.1016/S1464-1895\(01\)00016-3](https://doi.org/10.1016/S1464-1895(01)00016-3)
- Haimson, B. C. (2002). True triaxial strength of the KTB amphibolite under borehole wall conditions and its use to estimate the maximum horizontal in situ stress. *Journal of Geophysical Research*, 107(B10), 2257. <https://doi.org/10.1029/2001JB000647>
- Haimson, B. C. (2003). Borehole breakouts in Berea sandstone reveal a new fracture mechanism. *Pure and Applied Geophysics*, 160(5), 813–831. <https://doi.org/10.1007/PL00012567>
- Haimson, B. C. (2007). Micromechanisms of borehole instability leading to breakouts in rocks. *International Journal of Rock Mechanics and Mining Sciences*, 44(2), 157–173. <https://doi.org/10.1016/j.ijrmmms.2006.06.002>
- Haimson, B. C., & Fairhurst, C. (1967). Initiation and extension of hydraulic fractures in rocks. *Society of Petroleum Engineers Journal*, 7(03), 310–318. <https://doi.org/10.2118/1710-PA>
- Haimson, B. C., & Klaetsch, A. (2007). Compaction bands and the formation of slot-shaped breakouts in St. Peter sandstone. *Geological Society, London, Special Publications*, 284(1), 89–105. <https://doi.org/10.1144/SP284.7>
- Haimson, B. C., & Kovacich, J. (2003). Borehole instability in high-porosity Berea sandstone and factors affecting dimensions and shape of fracture-like breakouts. *Engineering Geology*, 69(3–4), 219–231. [https://doi.org/10.1016/S0013-7952\(02\)00283-1](https://doi.org/10.1016/S0013-7952(02)00283-1)
- Haimson, B. C., & Lee, H. (2004). Borehole breakouts and compaction bands in two high-porosity sandstones. *International Journal of Rock Mechanics and Mining Sciences*, 41(2), 287–301. <https://doi.org/10.1016/j.ijrmmms.2003.09.001>
- Haimson, B. C., & Song, I. (1993). Laboratory study of borehole breakouts in Cordova Cream: A case of shear failure mechanism. *International Journal of Rock Mechanics and Mining Sciences*, 30(7), 1047–1056. [https://doi.org/10.1016/0148-9062\(93\)90070-T](https://doi.org/10.1016/0148-9062(93)90070-T)
- Haimson, B. C., & Song, I. (1998). Borehole breakouts in Berea sandstone: Two porosity-dependent distinct shapes and mechanisms of formation. In *Proceedings of the SPE/ISRM Rock Mechanics in Petroleum Engineering, 8–10 July 1998* (pp. 229–238). Trondheim, Norway: Society of Petroleum Engineers. <https://doi.org/10.2118/47249-MS>
- Issen, K. A., & Rudnicki, J. W. (2000). Conditions for compaction bands in porous rock. *Journal of Geophysical Research*, 105(B9), 21,529–21,536. <https://doi.org/10.1029/2000JB900185>
- Lee, M., & Haimson, B. C. (1993). Laboratory study of borehole breakouts in Lac du Bonnet granite: A case of extensile failure mechanism. *International Journal of Rock Mechanics and Mining Sciences*, 30(7), 1039–1045. [https://doi.org/10.1016/0148-9062\(93\)90069-P](https://doi.org/10.1016/0148-9062(93)90069-P)
- Lee, H., Moon, T., & Haimson, B. C. (2016). Borehole breakouts induced in Arkosic sandstones and a discrete element analysis. *Rock Mechanics and Rock Engineering*, 49(4), 1369–1388. <https://doi.org/10.1007/s00603-015-0812-0>
- Liu, Y., Sun, W., Yuan, Z., & Fish, J. (2016). A nonlocal multiscale discrete-continuum model for predicting mechanical behavior of granular materials. *International Journal for Numerical Methods in Engineering*, 106(2), 129–160. <https://doi.org/10.1002/nme.5139>
- Ljunggren, C., Chang, Y., Janson, T., & Christiansson, R. (2003). An overview of rock stress measurement methods. *International Journal of Rock Mechanics and Mining Sciences*, 40(7–8), 975–989. <https://doi.org/10.1016/j.ijrmmms.2003.07.003>
- Muller, A. L., Vargas, E. d. A., Vaz, L. E., Figueiredo, R. P., & Gonçalves, C. J. (2011). Numerical analysis of sand/solids production in boreholes considering fluid-mechanical coupling in a Cosserat continuum. *International Journal of Rock Mechanics and Mining Sciences*, 48(8), 1303–1312. <https://doi.org/10.1016/j.ijrmmms.2011.09.012>
- Nitka, M., Combe, G., Dascalu, C., & Desrués, J. (2011). Two-scale modeling of granular materials: A DEM-FEM approach. *Granular Matter*, 13(3), 277–281. <https://doi.org/10.1007/s10035-011-0255-6>
- Olsson, W. A. (1999). Theoretical and experimental investigation of compaction bands in porous rock. *Journal of Geophysical Research*, 104(B4), 7219–7228. <https://doi.org/10.1029/1998JB900120>
- Olsson, W. A., Holcomb, D. J., & Rudnicki, J. W. (2002). Compaction localization in porous sandstone: Implications for reservoir mechanics. *Oil & Gas Science and Technology*, 57(5), 591–599. <https://doi.org/10.2516/ogst:2002040>

- Ong, S. H., & Roegiers, J. C. (1993). Influence of anisotropies in borehole stability. *International Journal of Rock Mechanics and Mining Sciences*, 30(7), 1069–1075. [https://doi.org/10.1016/0148-9062\(93\)90073-M](https://doi.org/10.1016/0148-9062(93)90073-M)
- Papanastasiou, P. C., & Vardoulakis, I. G. (1992). Numerical treatment of progressive localization in relation to borehole stability. *International Journal for Numerical and Analytical Methods in Geomechanics*, 16(6), 389–424. <https://doi.org/10.1002/nag.1610160602>
- Rahmati, H., Nouri, A., Chan, D., & Vaziri, H. (2014). Simulation of drilling-induced compaction bands using discrete element method. *International Journal for Numerical and Analytical Methods in Geomechanics*, 38(1), 37–50. <https://doi.org/10.1002/nag.2194>
- Reinecker, J., Tingay, M. R. P., & Müller, B. B. (2003). Borehole breakout analysis from four-arm caliper logs. World Stress Map Project, 1–5. Retrieved from [http://extra.springer.com/2010/978-1-4020-8443-0/WSM\\_Release\\_2008/WSM\\_website/pub/guidelines/WSM\\_analysis\\_guideline\\_breakout\\_caliper.pdf](http://extra.springer.com/2010/978-1-4020-8443-0/WSM_Release_2008/WSM_website/pub/guidelines/WSM_analysis_guideline_breakout_caliper.pdf)
- Santarelli, F. J., & Brown, E. T. (1989). Failure of three sedimentary rocks in triaxial and hollow cylinder compression tests. *International Journal of Rock Mechanics and Mining Sciences*, 26(5), 401–413. [https://doi.org/10.1016/0148-9062\(89\)90936-4](https://doi.org/10.1016/0148-9062(89)90936-4)
- Santarelli, F. J., Brown, E. T., & Maury, V. (1986). Analysis of borehole stresses using pressure-dependent, linear elasticity. *International Journal of Rock Mechanics and Mining Sciences*, 23(6), 445–449. [https://doi.org/10.1016/0148-9062\(86\)92310-7](https://doi.org/10.1016/0148-9062(86)92310-7)
- Schmitt, D. R., Currie, C. A., & Zhang, L. (2012). Crustal stress determination from boreholes and rock cores: Fundamental principles. *Tectonophysics*, 580, 1–26. <https://doi.org/10.1016/j.tecto.2012.08.029>
- Sheets, R. J., & Haimson, B. C. (2004). Drilling variables affecting fracture-like borehole breakout characteristics. In Gulf Rocks 2004, the 6th North America Rock Mechanics Symposium (NARMS).
- Shen, B., Stephansson, O., & Rinne, M. (2002). Simulation of borehole breakouts using FRACOD2D. *Oil & Gas Science and Technology*, 57(5), 579–590. <https://doi.org/10.2516/ogst.2002039>
- Tembe, S., Baud, P., & Wong, T.-F. (2008). Stress conditions for the propagation of discrete compaction bands in porous sandstone. *Journal of Geophysical Research*, 113, B09409. <https://doi.org/10.1029/2007JB005439>
- Wang, K., & Sun, W. (2016). A semi-implicit discrete-continuum coupling method for porous media based on the effective stress principle at finite strain. *Computer Methods in Applied Mechanics and Engineering*, 304, 546–583. <https://doi.org/10.1016/j.cma.2016.02.020>
- Wong, T.-F., David, C., & Zhu, W. (1997). The transition from brittle faulting to cataclastic flow in porous sandstones: Mechanical deformation. *Journal of Geophysical Research*, 102(B2), 3009–3025. <https://doi.org/10.1029/96JB03281>
- Wu, H., Guo, N., & Zhao, J. (2017). Multiscale modeling and analysis of compaction bands in high-porosity sandstones. *Acta Geotechnica*. <https://doi.org/10.1007/s11440-017-0560-2>
- Zervos, A., Papanastasiou, P. C., & Vardoulakis, I. G. (2001). Modelling of localisation and scale effect in thick-walled cylinders with gradient elastoplasticity. *International Journal of Solids and Structures*, 38(30–31), 5081–5095. [https://doi.org/10.1016/S0020-7683\(00\)00337-1](https://doi.org/10.1016/S0020-7683(00)00337-1)
- Zhang, J. (2013). Borehole stability analysis accounting for anisotropies in drilling to weak bedding planes. *International Journal of Rock Mechanics and Mining Sciences*, 60, 160–170. <https://doi.org/10.1016/j.ijrmms.2012.12.025>
- Zhang, J., Bai, M., & Roegiers, J. C. (2003). Dual-porosity poroelastic analyses of wellbore stability. *International Journal of Rock Mechanics and Mining Sciences*, 40(4), 473–483. [https://doi.org/10.1016/S1365-1609\(03\)00019-4](https://doi.org/10.1016/S1365-1609(03)00019-4)
- Zhao, J., & Guo, N. (2015). The interplay between anisotropy and strain localisation in granular soils: A multiscale insight. *Géotechnique*, 65(8), 642–656. <https://doi.org/10.1680/geot.14.P.184>
- Zheng, Z., Kemeny, J., & Cook, N. G. W. (1989). Analysis of borehole breakouts. *Journal of Geophysical Research*, 94(B6), 7171. <https://doi.org/10.1029/JB094iB06p07171>
- Zoback, M. D., Moos, D., Mastin, L., & Anderson, R. N. (1985). Well bore breakouts and in situ stress. *Journal of Geophysical Research*, 90(B7), 5523–5530. <https://doi.org/10.1029/JB090iB07p05523>